The Astronomical Journal, 136:2083–2101, 2008 November doi:10.1088/0004-6256/136/5/2083

THE DISTRIBUTION AND PROPERTIES OF COLD DUST IN NGC 6334

Henry E. Matthews[1,2], William H. McCutcheon[3], Helen Kirk[1,4], Glenn J. White[5,6], and Martin Cohen[7]
[1] National Research Council Canada, Herzberg Institute of Astrophysics, 5071 West Saanich Rd, Victoria, BC V9E 2E7, Canada; henry.matthews@nrc-cnrc.gc.ca
[2] National Research Council Canada, Herzberg Institute of Astrophysics, DRAO, P.O. Box 248, White Lake Road, Penticton, BC V2A 6J9, Canada
[3] University of British Columbia, Department of Physics & Astronomy, Vancouver, BC V6T 1Z1, Canada
[4] Department of Physics & Astronomy, University of Victoria, Victoria, BC V8P 1A1, Canada
[5] Department of Physics and Astronomy, The Open University, Walton Hall, Milton Keynes, MK7 6AA, UK
[6] Science & Technology Facilities Council, Rutherford Appleton Laboratory, Harwell Science and Innovation Campus, Didcot, OX11 0QX, UK
[7] Radio Astronomy Laboratory, University of California, Berkeley, CA 94720, USA
Received 2008 May 15; accepted 2008 August 27; published 2008 October 13

ABSTRACT

NGC 6334 is a galactic star-forming region in Scorpius, heavily obscured by intervening dust. The region consists of several major sites of star formation known previously from far-infrared (IR) and radio-wavelength observations. We present images of NGC 6334 obtained at wavelengths of 850 and 450 μm with the Submillimeter Common-User Bolometric Array at the James Clerk Maxwell Telescope. These data highlight the distribution of dense cold dust, a particularly striking feature of which is a narrow ridge of emission passing between most of the star-forming centers. We use a clump-finding technique to quantify the distribution of dust emission throughout the region, and we obtain estimates of the sizes, masses, and temperatures of the clump ensemble under simple assumptions. Clump masses range from a minimum detectable of about 1 $M_{\odot}$, up to almost 3000 $M_{\odot}$. We find in particular that the ridge feature is characterized by a relatively narrow range of clump parameters as compared with the rest of NGC 6334, and we obtain a clump mass spectral index that lies between $N(M) \propto M^{-1.5}$ and $M^{-1.0}$ for the high-mass clumps. The total mass of dust emitting at submillimeter wavelengths is about 16700 $M_{\odot}$ for an assumed temperature of 25 K; a significant fraction of this mass is contained within the ridge feature. These data are compared with recently published observations of NGC 6334 obtained at 1.2 mm wavelength using a direct-detection scanning technique, and with images obtained by the GLIMPSE-II and *Midcourse Space Experiment* missions at wavelengths from 3.3 to 21 μm in the near IR (NIR). The most massive compact submillimeter-wavelength regions in the north are invisible at these shorter wavelengths, and the NIR and mid-IR emission generally have little correspondence with the cool dust distribution. In this paper we use these data sets and supplementary millimeter-wavelength spectral line observations to investigate the star-forming sites in NGC 6334 and to speculate on the significance of the ridge of material seen in the submillimeter images.

Key words: ISM: clouds – ISM individual (NGC 6334) – ISM: structure – radio continuum: ISM – stars: formation – techniques: image processing

1. INTRODUCTION

NGC 6334 is a star-formation region south of the Galactic Center at $\ell, b \sim 351.3, -0\overset{\circ}{.}7$ in Scorpius at a distance of 1.7 ± 0.3 kpc (Neckel 1978). The region is heavily obscured at optical wavelengths, but early mid-infrared (MIR) and radio-wavelength mapping observations (Loughran et al. 1986; Rodríguez et al. 1982) of the region revealed six embedded star-forming regions extending over a projected distance of about 10 pc. NGC 6334 has subsequently been the target of numerous studies that penetrate the intervening dust; for example, in the IR (Burton et al. 2000) and the MIR and far-IR (FIR; Kraemer et al. 2000, 1999, respectively). These studies already demonstrated pervasive star formation throughout the region, with photodissociation regions about 1.0–1.5 pc in diameter surrounding ionized gas bubbles, and coincident with filamentary polycyclic aromatic hydrocarbon (PAH) emission.

It is tempting to speculate on the possibility of an evolutionary sequence in NGC 6334, in the sense that the northeastern regions are the more massive and centrally concentrated, and hence probably younger than those to the southwest. The northernmost region, including sources I and I(N) (using the nomenclature of Loughran et al. 1986), contains highly embedded objects visible only at submillimeter wavelengths, and source I rivals IRC2 in the Orion Molecular Cloud in terms of its molecular complexity and outflow activity. Sources II–V (at the southern end of NGC 6334) exhibit a variety of characteristics, and may be more evolved.

In this paper we present images of continuum emission in NGC 6334 at two submillimeter wavelengths (850 and 450 μm). The emission arises almost entirely from dust particles which are typically about 0.1 μm in size (Désert et al. 1990); since the emission is optically thin under all but the most extreme circumstances, the present observations reveal the distribution of cold dust within the observed region. The negative aspect of the low optical depth in dust is of course that the observed signals are quite weak. Nevertheless, since the observations have been carried out at two wavelengths, we are also able to obtain crude estimates of the dust temperature. We compare these results with data obtained in the MIR by the *Midcourse Space Experiment* (*MSX*) satellite mission and the more recent GLIMPSE-II survey, and also with molecular line-mapping observations of the 2–1 rotational transitions of CO and its common isotopomers. The latter images and analysis will be published in a separate paper (W. H. McCutcheon et al. 2008, in preparation) focused on the molecular aspects of NGC 6334.

Parts of NGC 6334 have been observed previously at submillimeter wavelengths. Images of sources I/I(N) appear in Gezari (1982) and Sandell (2000), and source IV was investigated by Sandell (1999), but the present images are the first to show the entire region with good sensitivity at these wavelengths. A recent paper (Muñoz et al. 2007) has examined NGC 6334 and the nearby NGC 6357 at a somewhat longer wavelength of 1.2 mm; we compare these results, where they overlap, with those presented in this paper.

2. OBSERVATIONS

The principal data reported here were obtained on 1998 June 26 and July 1 with the bolometer array camera Submillimeter Common-User Bolometric Array instrument (SCUBA; Holland et al. 1999) deployed on the James Clerk Maxwell Telescope (JCMT). The observations were made simultaneously in the two primary wavebands, centered at 850 and 450 μm, in the chop/scan mapping mode, as was commonly used for SCUBA observations of extended fields.

In this observing method the telescope was scanned across the target field at a rate of 24 arcsec s^{-1} while the secondary mirror was nutated in the R.A./decl. frame at 7.8125 Hz. Each scan covers an area of sky slightly more than 2′ wide (i.e., the instantaneous field of view of the bolometer array), and the region was observed using a series of overlapping scans in order to cover the complete field. The scanning was performed in Nasmyth coordinates, arranged with respect to the projection of the array on the sky such that the image is fully sampled. As was normal for this mode, six chop throw/direction combinations were used to provide full sampling (three nutator chop throws of 20″, 30″, and 65″ in each of two orthogonal chop-throw directions). This technique (e.g., Jenness et al. 2000) is a variant of mapping techniques in use for many years at other facilities, adapted to the challenging conditions that result from observing at submillimeter wavelengths through an atmosphere possessing both substantial optical depth and significant variability.

NGC 6334 was observed in three overlapping sections each nominally 10′ on a side, although in practice in the chop/scan-mapping mode useful data were obtained for about 1′ beyond the nominal observing region boundary. Also, because of the southern declination of NGC 6334 (about $-36°$) the observations were restricted to within ±2 hr of transit in order to obtain good results at both observing wavelengths. Sky conditions were good, but not exceptional, during the observing; the zenith optical depth monitored at 225 GHz[8] was quite stable at about 0.075 and 0.056 on June 26 and July 1 respectively, with sub-arcsecond seeing throughout. The zenith optical depths at 850 and 450 μm are respectively factors of about 4.0 and 23.5 times greater than those measured at 225 GHz. Since the air masses ranged between 1.77 at transit up to 2.46 actual line-of-sight optical depths at 850 μm lie between 0.4 and 0.7, and at 450 μm between 2.2 and 4.3. Observations at 450 μm are challenging even under the good conditions available to this program.

In this paper we also make use of $C^{18}O$ (2–1) spectral line imaging observations of NGC 6334, which were obtained in 1997 using a single-beam heterodyne receiver at the JCMT with a beam width somewhat larger (22″) than that of the current submillimeter-wavelength continuum data.

In order to estimate the gas temperature, we made supplementary observations in service mode with the JCMT in 2002 August at a series of 12 points along the ridge of NGC 6334 using observations of H_2CO. For these, the ($3_{03} - 2_{02}$) and ($3_{22} - 2_{21}$) transitions at 218 GHz were observed simultaneously within the same receiver bandpass by splitting the auto-correlation spectrometer used into two narrow windows centered on each line. A third spectral line, CH_3OH ($4_{23} - 3_{13}$), appears in this observing band and is positively detected at the six most northern positions (see Table 2). Since these lines are also close in the rest frequency to the $C^{18}O$ (2–1) transition, all four spectral lines observed in this program share the same telescope beam and efficiency parameters. Thus the ratios between the integrated line intensities can be used to provide meaningful physical information (see Mangum & Wootten 1993). In particular, the two H_2CO transitions have upper state excitation levels of 21 and 68 K respectively, and hence the ratio of the line intensities is sensitive to gas with T_{ex} of a few times 10 K.

[8] Available from the nearby Caltech Submillimeter Observatory.

3. DATA REDUCTION

The difficult conditions, largely the result of the low elevation angle of NGC 6334, under which the submillimeter-wavelength continuum observations were obtained in turn prompted careful data reduction, especially in view of the limited amount of data available; these are the only scan-map data obtained for this target with the SCUBA. The initial stages of the data reduction were carried out using standard programs that are included in the SCUBA data reduction tools, and implemented via the ORAC-DR data reduction package (Jenness & Economou 1999). Bolometers were excluded from the data set over intervals when they exhibited noise levels of instrumental origin substantially in excess of the normal values under the circumstances. Also, two bolometers in the 450 μm array were omitted entirely, as they appear to have been electronically linked since the inception of SCUBA in 1996 (see the JCMT Web pages).

Data from both observing sessions were combined at 850 μm, weighted according to the noise in the individual data sets. For the 450 μm data set, only the July 1 data were included, as the sky transmission at this wavelength in particular was substantially worse on June 26. All data were processed using tools provided via the ORAC-DR pipeline up to, and including, the sky-correction stage.

These sky-corrected data were then processed in two complementary ways, in order to assess the likely reality of weaker structures in the final images. We used both the standard Emerson–Klein–Haslam rebinning/dual-beam-removal deconvolution method (Emerson et al. 1979) incorporated within the SURF data reduction package, and also an implementation of the matrix-inversion technique (Johnstone et al. 2000) at the Joint Astronomy Centre Hawaii (JACH). One particular advantage of the latter method is that maps of the noise statistics are produced along with the image. The initial results from both data reduction methods, presented in this paper, result in very similar images. On balance we prefer the matrix-inversion data sets, and these versions are used exclusively in the rest of this paper.

The data were calibrated using observations of Uranus obtained concurrently using the same observing and data reduction techniques as for those of NGC 6334. The calibration of Uranus is in turn based on that of Mars, for which the behavior of the brightness temperature summed over the planetary disk has been derived using a temporal extension of a model of the Martian brightness temperature (Wright 1976; see also Privett et al. 2005). From the Uranus observations the beamwidths (full width to half-power) were determined to be 13.5 and 8″.5 at 850 and 450 μm, respectively, and the derived gain factors were found to be 195 and 690 Jy beam^{-1} V^{-1} at these two wavelengths.

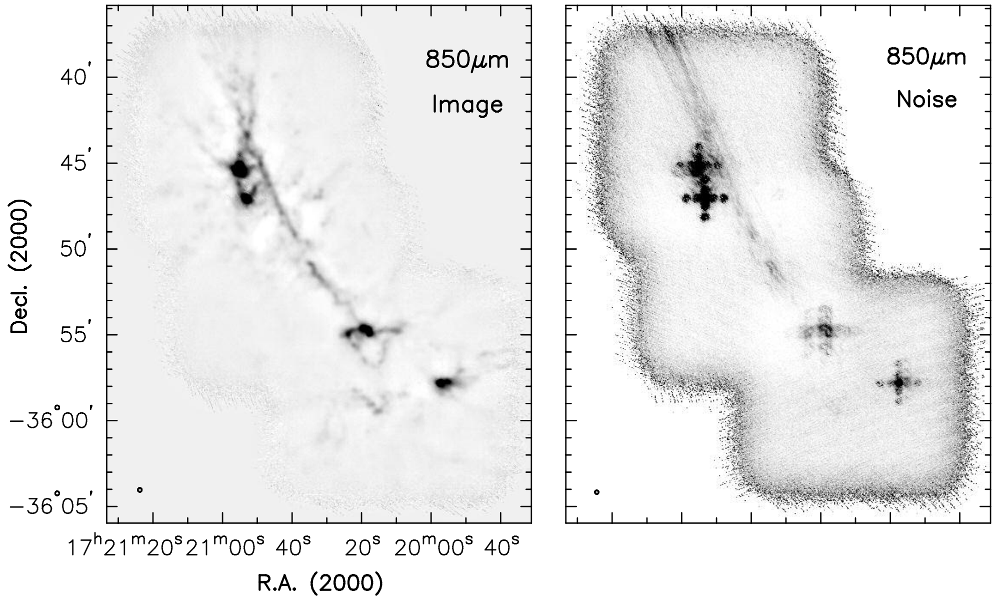

Figure 1. NGC 6334 at 850 μm; the image (left), and the noise distribution (right), from the image reconstruction using the matrix inversion technique (see the text). The gray-scale ranges (white to black) displayed are −0.5 to 8.0 and 0.04–0.25 Jy beam^{-1} for the image and noise maps, respectively. In general, the noise is fairly uniform across the mapped region, except near the edges, where there are fewer sampled points per beam. Excessive noise also occurs at the locations of the brighter sources, in this case from Poisson noise. The beam size to half-power (13.″5) is represented by the small circle at lower left in each frame.

Both the standard rebinning/dual-beam-removal data reduction method and the matrix inversion technique require that the sum of the flux density be set to zero, resulting in artificial negative bowl structures in the image on angular scales greater than those sampled. There are also instrumental negative-intensity features resulting from the chopping technique used, which are especially evident close to the strong sources of emission, and in particular near sources I and I(N). In order to mitigate these effects we applied a simple unsharp mask 2′ in width to remove larger-scale structures in both reduced data sets. Since structures larger than the maximum chop throw of 68″ in both dimensions are not represented in these data, this approach does not remove a significant fraction of the flux observed from the source. For each of the 450 and 850 μm dual-beam and matrix-inversion data sets, we first clipped the images at intensity levels that included only the larger-scale low-level structure, and smoothed the remaining data with a Gaussian of full width at half-maximum (FWHM) of 2′. The resultant data sets were then subtracted from the initial images. The flux from the region is not completely recorded for extended emission, as the chopping technique employed is not sensitive in particular to smooth two-dimensional structures larger than the maximum chop throw. However, filamentary structures of any size within the mapped area will be fully registered, as the chop/scan method involves chopping the subreflector in two directions and with three different throws (see Section 2).

The results of the matrix-inversion data reduction are shown in Figures 1 and 2 for the 850 and 450 μm data sets, respectively. We display the reconstructed images and noise maps in each case. The latter clearly show the extent of the valid data. The rms noise levels in the final images are typically in the range of 8 to 13 mJy beam^{-1} at 850 μm. The average value for the 450 μm image is about 300 mJy beam^{-1}, although it ranges from 200 mJy beam^{-1} in the overlap regions to 430 mJy beam^{-1} in the southernmost segment, observed as NGC 6334 was setting. Note that the pixels in both the 850 and 450 μm maps subsample the beam, so that the noise per pixel is several times larger than that per beam.

The implementation of matrix inversion used here provides a map also of the number of valid data points used per pixel. The latter varies significantly over the imaged regions; in the present case, for the 850 μm data set it ranges from about 40 over most of the map to about 75 in the overlap regions of adjacent fields. For the 450 μm data set, the lowest numbers, of about 45, occur in the central region, the highest numbers, typically 95, occur in the overlap regions, and in the northern fields there are about 55 data points per pixel.

In Figure 3 we compare the low-level structure in the images of the region processed using matrix-inversion and dual-beam removal techniques. The detailed structure is closely reproduced in both images at levels down to the statistical noise, indicating that these structures are essentially independent of the image reconstruction method. The unsharp masking technique is unable to remove some of the more negative features close to the brighter components, as apparent in these maps. In the rest of this paper we use the matrix-inverted data.

4. STRUCTURES IN COLD DUST

Figure 4 summarizes the relationship between the present observations and early observations which first revealed the presence of a massive and heavily obscured star-forming region in NGC 6334. The radio-wavelength sources (designated F–A, from north to south) and those observed at FIR wavelengths (sources I/I(N)–V) are clearly distributed similarly to that of the dense cool dust material seen in the present submillimeter-wavelength images. Additionally, of the eight compact objects found in the *IRAS* Point Source Catalog (PSC) within this region, four are also coincident within the errors with the principal FIR sources. Sources I(N) and IV are not associated with *IRAS*-PSC objects, and the remaining four *IRAS*-PSC objects do not have counterparts in the submillimeter-wavelength images, and may be extragalactic in nature.

At optical wavelengths NGC 6334 is very heavily obscured (see Figure 5 for an overlay of 850 μm emission contours on an optical image of the region), and the structures seen bear

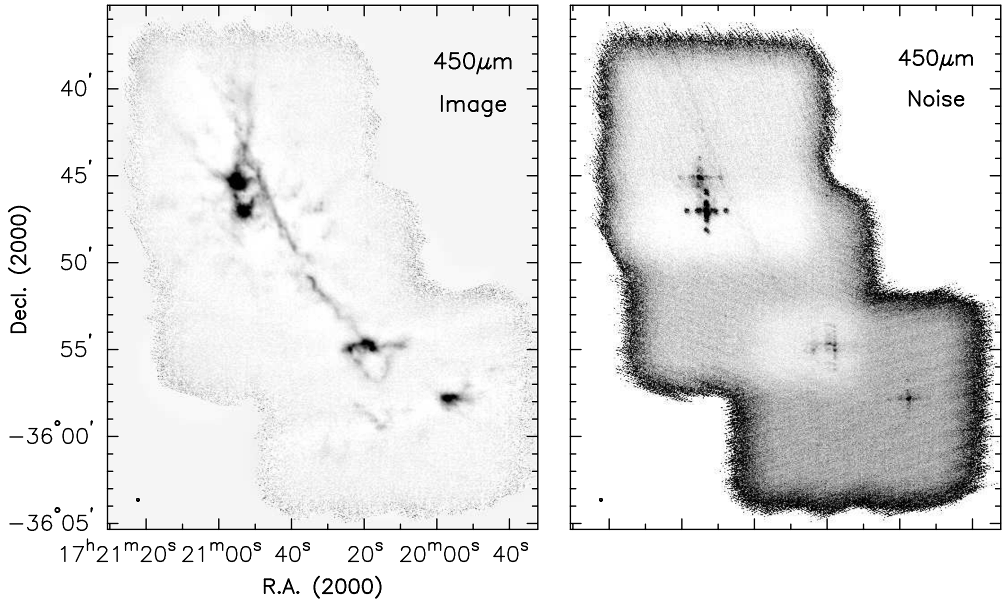

Figure 2. NGC 6334 at 450 μm; the image (left), and the noise distribution (right), from the image reconstruction using matrix inversion. These data were obtained from a series of observations on a single morning (1998 July 1). The evident increase in the background noise at lower declinations results from increasing sky noise as the source was setting while the observations progressed. The gray-scale ranges are -1.5 to 45.0 and 0.7 to 2.5 Jy beam^{-1} for the image and noise maps, respectively. The beamwidth to half-power (in the lower left) is 8$''$.5. Other details are as in Figure 1.

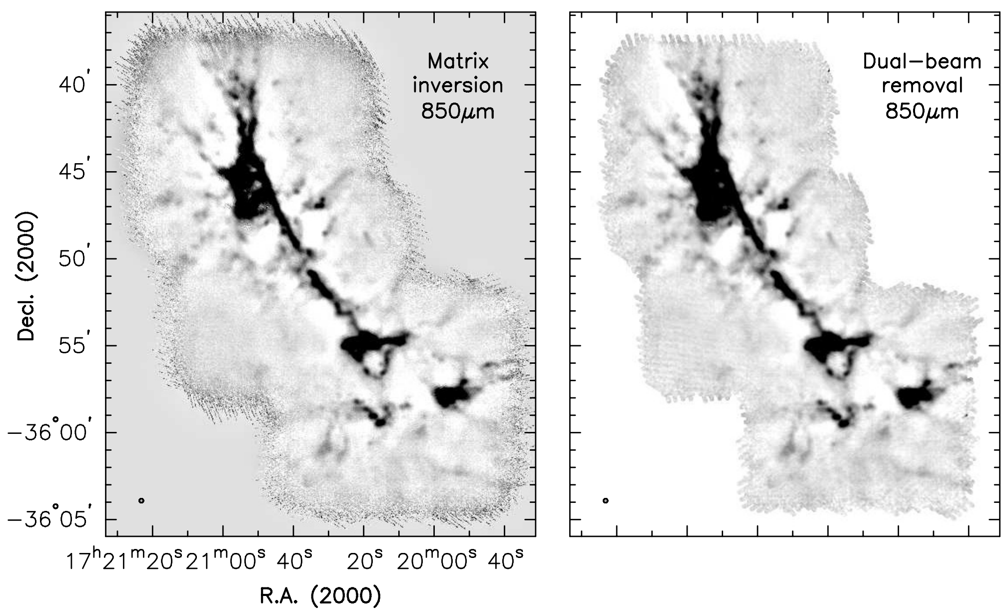

Figure 3. A comparison of the images showing the low-intensity structure of the NGC 6334 region at 850 μm wavelength, processed using the matrix-inversion (left) and the dual-beam removal (right) techniques. The gray-scale range is -0.2 to 1.5 Jy beam^{-1} for both images; emission greater than 1.5 Jy beam^{-1} is saturated in this image. Other details are as in Figure 1.

no relation to those seen at submillimeter wavelengths. This was apparent already from early radio-IR and FIR observations of the region by Rodríguez et al. (1982) and Loughran et al. (1986) respectively, which indicated the presence of several centers of previously unknown active OB star formation.

4.1. Overall Dust Emission Structure

The images in this paper, e.g., Figure 4, highlight the prominent dust ridge with a high length-to-width ratio that extends throughout most of the observed region. Beginning at FIR source IV this structure traverses northeast with some localized deviations past the FIR objects I and I(N), where it appears to bifurcate, both strands perhaps continuing to the northern edge of the image. Most of the MIR/FIR sources, I, I(N), III, IV, and V, are themselves closely associated with dust emission at submillimeter wavelengths. FIR source II is alone in having no such association. Other large-scale features appear in the image, in particular a loop of dust emission south of source IV.

The LSR velocity centroid of the associated molecular line emission in NGC 6334 (see Section 8.1) remains within a few km s^{-1} of -2.5 km s^{-1} throughout the entire region; this strongly suggests that the ridge of emission and the clumped dust emission are co-spatial, and hence potentially coeval structures.

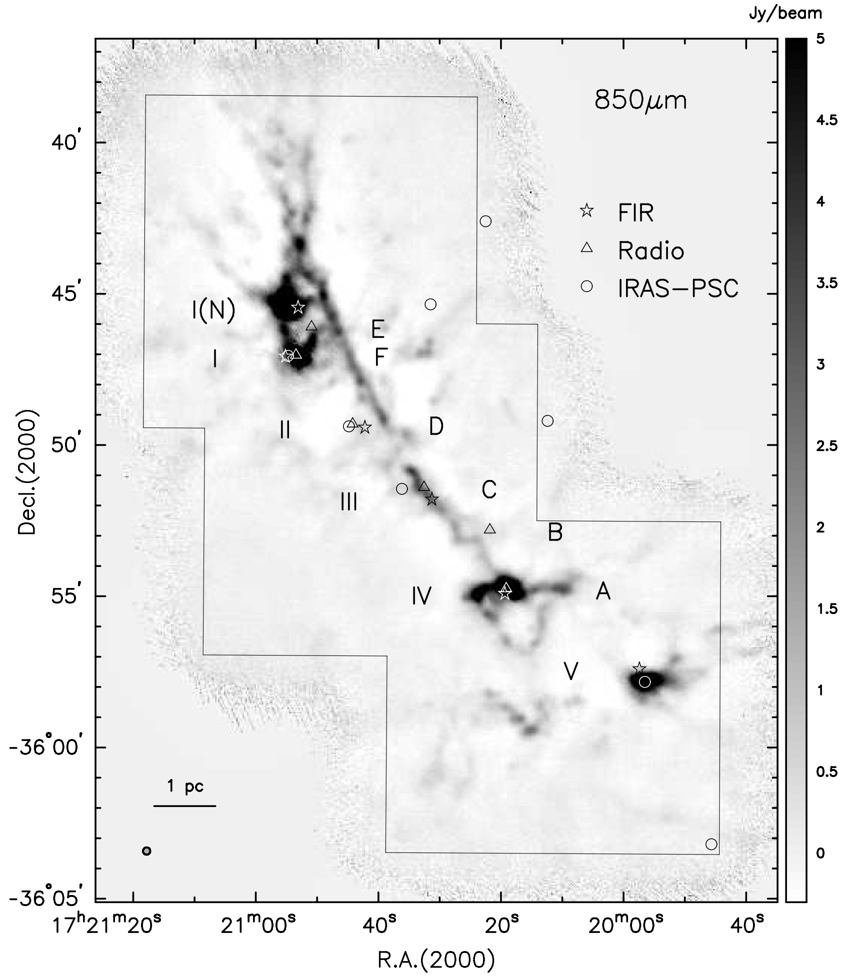

Figure 4. The 850 μm image of NGC 6334 overlaid with the locations of compact MIR to FIR objects and radio wavelength sources (indicated by star and triangle symbols, respectively; see key in the upper right) discovered in early surveys. The FIR source names I(N) and I–V (see Loughran et al.1986) are given to the left, while the radio source names A–F are given to the right, of the corresponding source positions (Rodríguez, et al., 1982). The positions of *IRAS*-PSC objects that lie within the mapped region are shown by the circles. The 850 μm image gray-scale range is -0.3 to 5 Jy beam^{-1}. The linear scale at the adopted distance of 1.7 kpc is indicated in the lower left. The outline border indicates the formal extent of the fully sampled data, although some real source structure extends beyond it into the noise at the edges. The slight rotation of the border outline results from the observations having been performed in the RB(1950) coordinate frame. Other details are as in Figure 1.

4.2. Other Structures

At lower emission levels, such as that shown in Figure 3, the images convey an impression of wind-driven structures directed away from the principal massive dust complexes throughout most of the region. Most of these are found in the vicinity of the I/I(N) complex, although there are some examples in the southern part of the region, notably to the west of source V. Another prominent feature lies to the south of source IV, in the form of a loop of emission containing a number of clumps.

In some cases, apparent head–tail structures are seen, such as those associated with the group of dust clumps about 4′ to the west of source I. This particular small group of sources is well resolved at 450 μm into individual components, and corresponds to the “cloudlet” observed at 1300 and 1100 μm by Sandell (2000). All of these objects have thermal dust spectra as determined from the present data set, with flux densities of typically 7–9 Jy and 1.0–1.5 Jy at 450 and 850 μm respectively, and appear to be superimposed on a region of more extended emission. If they are at the same distance as the body of NGC 6334 these objects are included within a projected area about 2 pc across. They may represent a separate small center of the ongoing star formation.

4.3. The Contribution of Spectral Line Emission

The 850 μm SCUBA observing band contains a considerable number of spectral lines arising in rotational transitions from molecules common in dense cold interstellar clouds. The principal contributors are CO (3–2) and HCN (4–3) (at 345.8 and 354.5 GHz; i.e., 828 and 846 μm, respectively); these and other more complicated species can contribute quite significantly to the apparent submillimeter continuum emission in the most extreme cases. Spectra of I and I(N), where this situation is likely to be most acute and the spectral contribution to the continuum may reach 40% of the total emission, are discussed extensively in McCutcheon et al. (2000). Later in this paper, in Section 8.1, we show that the distribution of molecular gas generally follows closely that of the cold dust component of the interstellar medium (ISM) of NGC 6334.

5. CLUMP ANALYSIS OF THE IMAGES

In order to quantify information from complex images such as those presented here, we require a method that extracts physical information from the data in a systematic and rigorous manner. A common approach is to decompose the images into a set of

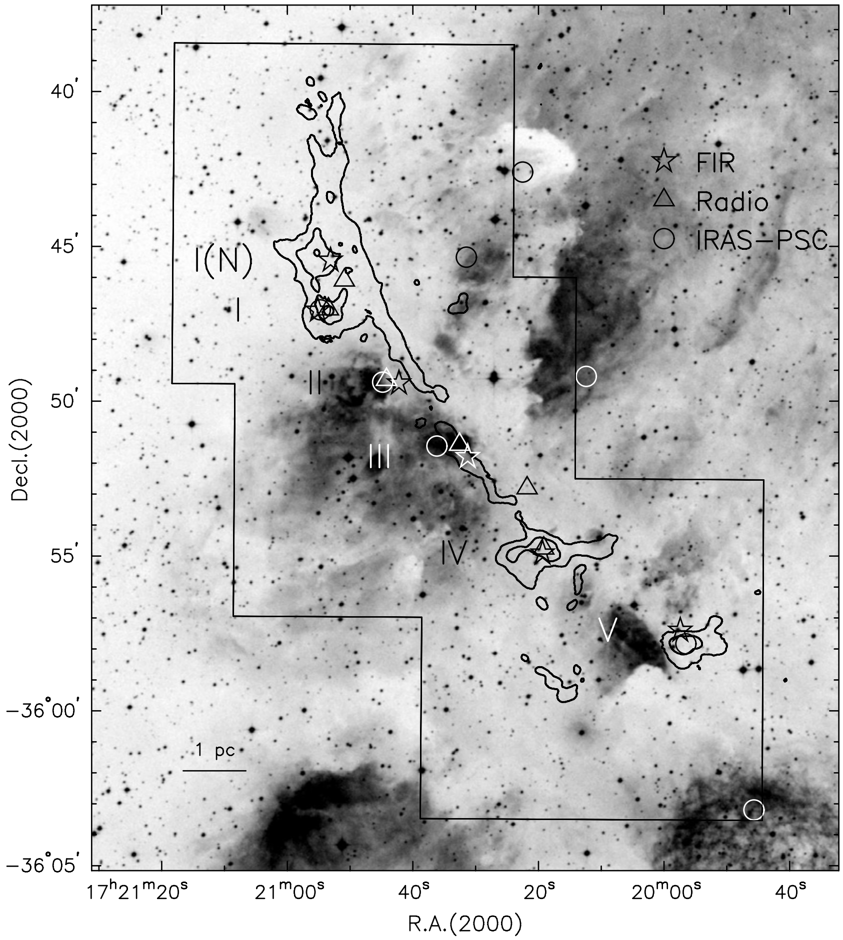

Figure 5. The distribution of cold dust in NGC 6334 (from the present work) in the context of an optical image of the region from the Sloan Digital Sky Survey (SDSS). Selected contours (1, 5, and 30 Jy beam^{-1}) from the 850 μm image are shown. Optically obscured compact IR, FIR, and radio wavelength sources known from early surveys are identified as in Figure 4. The submillimeter-wavelength objects clearly bear little relation to structures seen in the optical image, attesting to the heavy obscuration in this region.

components in recognition of the inherently clumped nature of the structure of interstellar clouds. Such a "clump analysis" is applied in the present instance; for this we used a two-dimensional version of the automated clump-finding algorithm `clfind` developed by Williams et al. (1994) and as used extensively by e.g., Johnstone et al. (2001) and others. In the implementation of `clfind` the shapes of individual clumps are not defined in advance; rather, each map cell in which the signal is greater than a given threshold value is assigned membership in a coherent substructure (or "clump") in the image, and clumps that achieve a minimum area consistent with the observing beam size are recognized as coherent physical entities.

We first applied this clump-finding approach separately to the matrix-inverted image reconstructions of the 850 and 450 μm data sets. Within about 2′ of the image edges (i.e., beyond the formal border of the observed region) the noise levels are substantially higher and these parts of the images were excluded from the object search. The results of this process are shown in Figure 6, where we identify the positions of the clumps found in the 850 and 450 μm data sets by circles and crosses respectively. Most of the brighter 850 μm clumps, in the main structures of NGC 6334, are also located in the 450 μm image. However, in some cases, the considerably smaller beamwidth of the 450 μm image causes single clumps at 850 μm to be subdivided at 450 μm. Further, although the thermal spectral index means that dust clumps are intrinsically brighter at 450 μm, this is outweighed by the considerably less good S/N at 450 μm compared with that of the 850 μm data. Thus a significant number of clumps seen at 850 μm cannot be detected at 450 μm.

The approach described above was not very satisfactory in view of the substantially different sensitivities for the 850 and 450 μm data sets. We therefore adopted an alternative strategy, in which we first applied `clfind` to the 850 μm image, and then used the clump boundaries determined from these data to estimate the peak and total fluxes of the equivalent features in the 450 μm image. We also determined the ratio of peak and total fluxes at 850 and 450 μm in order to estimate the dust temperature for each clump (see Section 6). In this calculation, it is important to take into account the beam profiles at both wavelengths. With these data, we created maps at both wavelengths which were then convolved with the beam profile of the other wavelength in order to obtain a fair measurement of the flux ratios. Reid & Wilson (2005) have carried out a careful study of SCUBA's beam profile at 850 and 450 μm; following Johnstone et al. (2006), and in view of the low declination of the present target, we make use of a simpler version of the beam profiles; here we assume that the 850 μm beam can be represented by two Gaussians of FWHM 14.″5 and 30″ with relative intensities of 0.95 and 0.05, respectively. Similarly, the 450 μm beam consists of two Gaussians of FWHM 8.″5 and

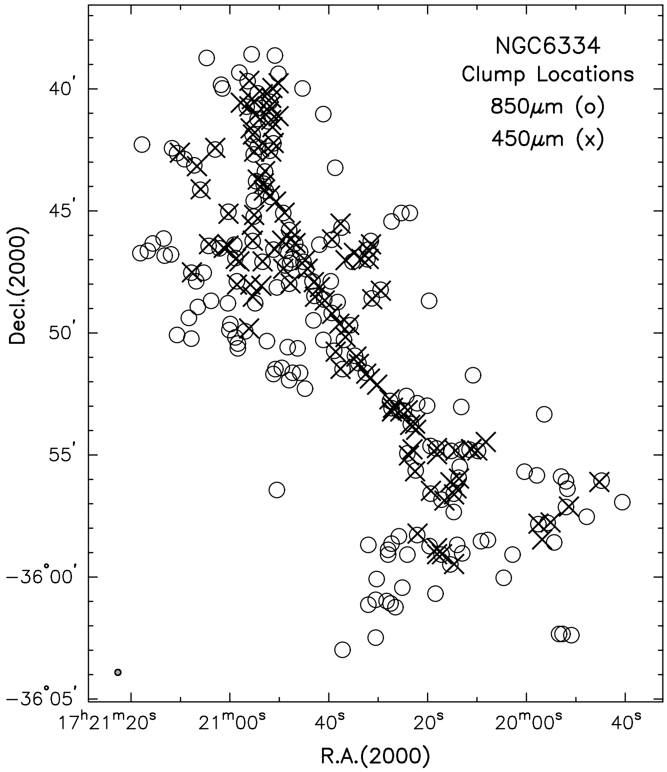

Figure 6. Clump positions, obtained by independent applications of `clfind` to the 850 and 450 μm images, indicated by circles and crosses, respectively. For the brighter clumps `clfind` generally obtains similar results at both 850 and 450 μm; however, the fainter objects are often not detected at 450 μm in such a blind search process; for this reason we adopted a hybrid approach to clump finding in order to obtain more consistent results (see Section 5).

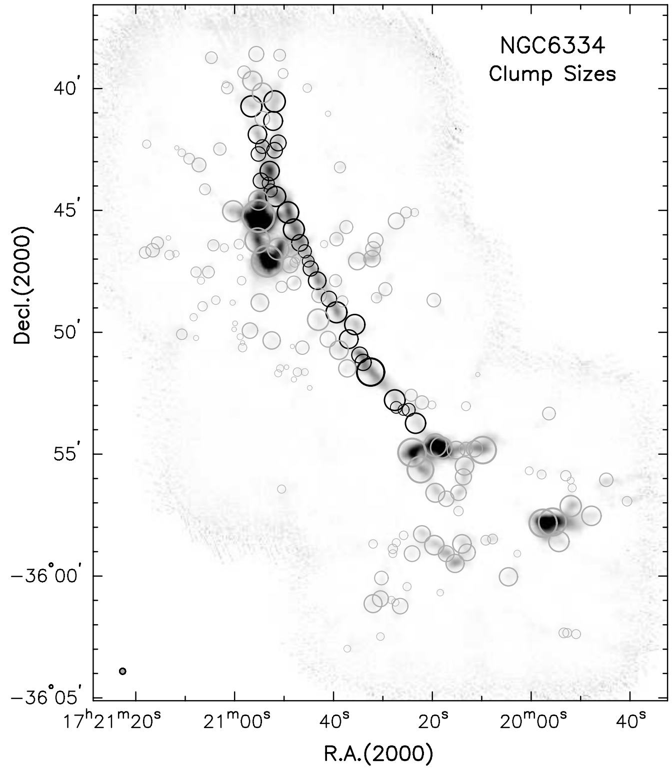

Figure 7. The distribution of dust clump sizes found in the NGC 6334 map. The sizes of the circles approximate those of the equivalent clump areas. The clumps which are associated with the prominent ridge of dust emission are shown by the black circles, and all others are shown in gray. The underlying image is the matrix-inverted map at 850 μm with a gray-scale range of 0–7 Jy beam^{-1}.

30″, also with relative intensities of 0.95 and 0.05, respectively. Although this may not be strictly applicable to the NGC 6334 data sets due to the low observing elevation at which the present data were obtained, it results in a data set which may be consistently compared to others processed in the same manner.

The results of the `clfind` analysis of these data sets are given in the first six columns of Table 1, listed in decreasing right ascension. The basic data obtained include the center position, peak, and total flux densities at 850 μm, and the clump size (in terms of the effective radius of the equivalent circular clump). A total of 168 clumps were positively identified. For 21 of these, the integrated flux density is less than the peak value; all of these clumps are quite small and faint, and the recorded flux density in such cases is often dominated by a single pixel with a relatively strong signal in the presence of a number of pixels with weak flux values.

These data are presented in Figure 7 superposed on a gray-scale image of the 850 μm emission from NGC 6334. In this image each clump is represented by a circle of area approximating that of the clump. The actual clump shapes found by `clfind` are generally not circular, and it is clear from Figure 7 that most clumps are parts of larger structures, often filamentary in overall appearance.

In our analysis below we differentiate clumps which appear to be part of the pronounced ridge of emission from those that are not. Later in this paper we show that the ranges of clump parameters appear to characterize this ridge as distinctly different from that of the larger part of the NGC 6334 region.

6. PHYSICAL PROPERTIES OF THE DUST CLUMP ENSEMBLE IN NGC 6334

The derived physical properties of the dust clumps are given in the second part of Table 1, in Columns 7–12. Having simultaneous measurements of the sky at the two frequencies in principle allows estimates of the temperature of the dust for each of the clumps. Assuming that the dust grains radiate as modified black bodies, the temperature can be calculated using (e.g., Reid & Wilson 2005):

$$R = \frac{S_{450}}{S_{850}} = \frac{e^{16.9/T} - 1}{e^{32.0/T} - 1}\left(\frac{850}{450}\right)^{3+\beta}, \quad (1)$$

where S is the flux at each wavelength, T is the temperature, and β is the dust emissivity index. We assume $\beta = 2$ and calculate temperatures using both the ratio of peak and integrated flux (T_p and T_s, respectively). As noted in Section 5, we compute fluxes using maps that have been convolved with the beam profile of the other wavelength so that both maps have the same beam profile. In practice the flux ratio is not very well determined if one takes into account the known sources of error in SCUBA measurements, particularly at 450 μm, where the error beam pattern and pointing uncertainties are significant factors.

In light of these sources of error, we anticipate uncertainties of roughly 50% in the flux density ratios. This large error prevents the accurate determination of temperatures, and is particularly limiting for the higher flux density ratios. A value for R of 8.5 is formally within errors of the ratio corresponding to the Raleigh–Jeans limit, i.e., temperatures greater than ∼22 K cannot be determined with any degree of certainty. The *relative* values of R (and hence T) are not so poorly constrained, however, since a

Table 1
Clumpfind Results for NGC 6334

Name[a]	R.A.[b]	Decl.[b]	Peak[c]	Total[c]	Radius[c]	Mass[d]	Concentration[c]	450/850 μm Ratio[e]		$T(p)$[e]	$T(s)$[e]
	(J2000)	(J2000)	(Jy beam^{-1})	(Jy)	(arcsec)	($M_\odot$)		Peak	Total	(K)	(K)
(1)	(2)	(3)	(4)	(5)	(6)	(7)	(8)	(9)	(10)	(11)	(12)
1	17:21:18.09	−35:46:43.96	0.50	0.97	14.9	11.5	0.43	14.9	14.1	60	60
2	17:21:17.81	−35:42:16.96	0.43	0.41	10.7	4.9	0.45	13.1	14.5	60	60
3	17:21:16.61	−35:46:38.01	0.61	1.75	17.5	20.8	0.39	13.6	14.7	60	60
4	17:21:15.62	−35:46:20.01	0.48	1.08	15.6	12.8	0.40	15.7	14.3	60	60
5	17:21:13.16	−35:46:50.07	0.40	0.52	12.1	6.2	0.42	17.5	17.7	60	60
6	17:21:11.94	−35:46:47.09	0.36	0.25	8.6	3.0	0.38	20.4	23.0	60	60
7	17:21:10.72	−35:50:05.10	0.63	1.08	13.7	12.9	0.39	12.5	12.1	60	60
8	17:21:10.66	−35:42:38.11	0.40	0.39	10.0	4.6	0.37	18.1	19.7	60	60
9	17:21:09.19	−35:42:53.15	0.46	0.81	14.0	9.7	0.41	13.6	16.6	60	60
10	17:21:08.25	−35:49:23.16	0.34	0.32	9.6	3.8	0.33	11.0	10.0	54	35
11	17:21:07.75	−35:47:32.17	0.47	0.78	13.4	9.2	0.40	15.1	14.3	60	60
12	17:21:07.22	−35:43:08.19	0.64	1.70	18.0	20.2	0.46	11.8	11.8	60	60
13	17:21:06.76	−35:47:53.17	0.35	0.28	9.4	3.3	0.41	16.6	12.6	60	60
14	17:21:06.52	−35:48:56.16	0.36	0.53	12.2	6.4	0.35	10.2	8.7	37	23
15	17:21:06.00	−35:44:08.19	0.62	1.01	14.2	12.0	0.47	11.5	11.7	60	60
16	17:21:05.28	−35:47:32.22	0.49	1.07	15.2	12.7	0.38	12.4	13.9	60	60
17	17:21:04.73	−35:38:44.21	0.60	1.06	15.2	12.6	0.50	6.3	2.8	14	7
18	17:21:04.29	−35:46:26.22	0.67	1.10	14.5	13.0	0.49	11.1	8.4	59	21
19	17:21:03.81	−35:48:41.22	0.30	0.40	11.1	4.7	0.30	14.0	11.9	60	60
20	17:21:03.03	−35:42:29.23	0.56	1.09	16.0	13.0	0.50	8.2	3.6	20	8
21	17:21:02.07	−35:46:32.24	0.38	0.40	10.7	4.8	0.39	22.2	23.4	60	60
22	17:21:01.79	−35:39:50.25	0.46	0.31	8.8	3.7	0.43	6.8	2.9	15	7
23	17:21:01.54	−35:39:59.25	0.55	0.96	14.9	11.4	0.49	8.0	4.1	19	9
24	17:21:00.34	−35:45:02.27	2.38	9.81	27.1	116.6	0.63	12.7	12.5	60	60
25	17:20:59.11	−35:46:23.28	0.45	0.61	12.7	7.2	0.45	9.9	21.2	33	60
26	17:20:58.63	−35:47:53.30	0.29	0.36	11.1	4.3	0.34	15.9	21.2	60	60
27	17:20:58.39	−35:50:38.30	0.37	0.39	11.0	4.6	0.43	15.0	11.3	60	60
28	17:20:58.09	−35:39:20.32	0.62	1.43	16.4	17.0	0.44	11.5	10.2	60	38
29	17:20:56.91	−35:49:56.32	0.63	1.98	20.0	23.6	0.48	12.9	11.6	60	60
30	17:20:56.62	−35:40:44.32	1.55	7.77	27.1	92.4	0.55	10.0	9.3	34	27
31	17:20:56.38	−35:39:41.31	1.38	4.67	24.9	55.5	0.64	10.7	11.7	48	60
32	17:20:55.63	−35:38:35.31	0.56	1.58	19.4	18.7	0.51	12.0	12.8	60	60
33	17:20:55.41	−35:46:14.32	6.10	36.73	31.9	436.5	0.61	14.1	12.4	60	60
34	17:20:55.39	−35:41:53.33	2.03	7.15	23.8	85.0	0.59	7.9	7.1	19	16
35	17:20:55.15	−35:44:35.34	6.42	25.63	25.3	304.6	0.59	13.9	12.6	60	60
36	17:20:55.15	−35:45:14.34	34.28	233.75	41.1	2777.8	0.74	10.7	12.2	47	60
37	17:20:55.15	−35:42:41.33	2.36	6.91	18.8	82.1	0.46	9.4	5.8	29	12
38	17:20:54.93	−35:48:47.35	0.72	2.87	22.8	34.0	0.50	18.9	18.6	60	60
39	17:20:54.66	−35:43:47.34	2.58	8.57	19.9	101.8	0.45	10.9	10.3	50	38
40	17:20:54.41	−35:42:23.33	2.67	6.33	17.7	75.2	0.50	6.9	6.8	15	15
41	17:20:54.41	−35:41:14.34	0.56	1.98	18.8	23.5	0.34	12.8	12.1	60	60
42	17:20:54.41	−35:40:11.35	1.06	5.46	25.7	64.8	0.49	14.0	14.0	60	60
43	17:20:53.44	−35:47:05.35	58.42	168.48	40.2	2002.1	0.88	11.0	12.7	55	60
44	17:20:53.18	−35:43:53.35	3.28	8.06	15.6	95.8	0.34	10.6	11.6	44	60
45	17:20:52.93	−35:43:23.36	5.94	23.62	24.8	280.7	0.58	9.8	10.4	32	40
46	17:20:52.69	−35:44:11.36	3.72	10.87	16.9	129.1	0.33	11.2	11.6	60	60
47	17:20:52.47	−35:50:20.35	0.50	2.04	22.4	24.3	0.47	9.2	7.6	27	18
48	17:20:52.19	−35:41:20.36	0.99	4.83	24.3	57.4	0.46	12.9	13.2	60	60
49	17:20:51.94	−35:42:32.37	2.95	8.53	20.2	101.4	0.53	8.3	8.8	21	24
50	17:20:51.93	−35:40:32.37	1.63	9.48	27.4	112.7	0.49	12.1	14.0	60	60
51	17:20:51.71	−35:44:26.35	4.31	19.24	25.8	228.6	0.56	10.8	10.9	48	51
52	17:20:51.24	−35:51:41.37	0.27	0.23	9.3	2.8	0.34	10.8	7.9	48	19
53	17:20:51.23	−35:46:35.38	6.16	32.68	27.7	388.4	0.55	15.5	13.1	60	60
54	17:20:51.21	−35:42:14.38	2.07	6.58	20.5	78.2	0.50	9.8	11.0	32	56
55	17:20:50.94	−35:38:38.36	0.52	1.00	15.2	11.8	0.46	14.9	16.5	60	60
56	17:20:50.75	−35:51:29.38	0.33	0.32	9.4	3.8	0.29	11.4	10.7	60	45
57	17:20:50.52	−35:56:26.38	0.41	0.41	10.7	4.9	0.42	13.2	9.6	60	30
58	17:20:50.49	−35:48:08.39	0.38	0.75	14.5	8.9	0.39	11.8	3.6	60	8
59	17:20:50.22	−35:39:23.38	0.28	0.48	12.8	5.7	0.31	20.0	20.9	60	60
60	17:20:49.24	−35:45:05.37	5.72	25.65	27.5	304.8	0.61	11.4	12.4	60	60
61	17:20:48.76	−35:47:14.39	1.71	6.17	20.7	73.4	0.45	14.7	11.3	60	60
62	17:20:48.51	−35:46:38.38	2.15	7.23	16.8	85.9	0.22	13.9	11.8	60	60

Table 1
(Continued)

Name[a]	R.A.[b]	Decl.[b]	Peak[c]	Total[c]	Radius[c]	Mass[d]	Concentration[c]	450/850 μm Ratio[e]		$T(p)$[e]	$T(s)$[e]
	(J2000)	(J2000)	(Jy beam^{-1})	(Jy)	(arcsec)	($M_\odot$)		Peak	Total	(K)	(K)
(1)	(2)	(3)	(4)	(5)	(6)	(7)	(8)	(9)	(10)	(11)	(12)
63	17:20:48.03	−35:47:59.41	1.01	2.01	18.2	23.9	0.61	10.1	8.4	35	22
64	17:20:48.02	−35:45:47.39	4.01	20.53	27.1	244.0	0.54	12.4	12.8	60	60
65	17:20:47.77	−35:47:08.40	1.46	1.69	12.5	20.0	0.52	9.4	8.2	28	20
66	17:20:47.53	−35:46:59.39	1.72	2.25	11.6	26.7	0.36	10.4	9.1	40	26
67	17:20:47.29	−35:51:38.39	0.47	0.53	11.1	6.3	0.40	7.3	4.6	17	10
68	17:20:46.79	−35:46:20.39	3.81	13.31	21.4	158.2	0.50	11.8	12.5	60	60
69	17:20:46.30	−35:50:38.41	0.42	1.09	17.2	12.9	0.43	11.0	5.8	54	13
70	17:20:45.81	−35:51:38.39	0.38	0.27	9.0	3.2	0.43	6.5	1.7	14	6
71	17:20:45.80	−35:46:41.40	2.43	6.41	17.0	76.2	0.40	11.7	11.2	60	60
72	17:20:45.29	−35:39:59.40	0.45	0.50	11.2	5.9	0.43	11.3	12.3	60	60
73	17:20:45.06	−35:47:05.41	2.73	5.49	15.3	65.2	0.44	10.9	10.6	53	44
74	17:20:44.57	−35:47:23.43	2.84	8.06	19.5	95.8	0.51	11.2	10.3	60	39
75	17:20:43.34	−35:47:53.42	3.35	10.99	22.7	130.6	0.58	11.3	11.2	60	60
76	17:20:43.10	−35:49:29.43	0.93	4.52	27.4	53.7	0.58	1.9	0.2	6	3
77	17:20:42.85	−35:48:29.41	1.89	5.67	19.1	67.4	0.46	11.3	8.8	60	24
78	17:20:41.85	−35:46:23.43	0.42	0.31	9.4	3.7	0.46	18.4	17.1	60	60
79	17:20:41.12	−35:50:17.41	0.35	1.58	20.5	18.8	0.29	7.2	1.6	16	6
80	17:20:40.87	−35:48:38.44	2.08	6.30	20.0	74.9	0.50	11.7	10.5	60	42
81	17:20:39.64	−35:47:53.42	0.66	1.18	15.8	14.0	0.53	13.4	5.0	60	11
82	17:20:39.39	−35:46:11.44	1.00	2.08	17.3	24.7	0.55	15.0	15.5	60	60
83	17:20:39.39	−35:49:11.42	3.26	13.47	27.0	160.1	0.63	11.5	9.4	60	28
84	17:20:38.89	−35:50:44.42	1.19	4.93	24.1	58.6	0.53	10.8	10.1	48	35
85	17:20:38.65	−35:43:14.42	0.76	0.97	14.4	11.5	0.60	9.8	9.9	32	33
86	17:20:38.16	−35:48:44.44	0.45	0.90	14.4	10.7	0.37	13.0	8.5	60	22
87	17:20:37.41	−35:45:41.45	0.58	1.45	16.8	17.2	0.42	12.6	10.6	60	44
88	17:20:37.18	−36:02:59.43	0.37	0.31	9.0	3.7	0.31	10.9	8.5	51	22
89	17:20:37.17	−35:51:29.44	0.65	2.76	22.3	32.8	0.44	9.3	10.4	27	40
90	17:20:36.92	−35:50:17.44	1.04	4.46	24.1	53.0	0.52	10.3	7.2	40	16
91	17:20:35.69	−35:49:41.43	1.83	7.51	26.1	89.2	0.61	10.3	9.7	39	31
92	17:20:35.20	−35:47:05.44	0.72	3.27	22.3	38.8	0.40	12.2	11.1	60	59
93	17:20:34.71	−35:50:56.42	3.87	9.26	20.6	110.0	0.63	12.4	11.9	60	60
94	17:20:33.97	−35:51:14.43	3.60	11.27	20.9	133.9	0.53	12.1	10.5	60	43
95	17:20:32.48	−35:51:38.43	3.21	23.45	35.5	278.7	0.62	10.7	9.8	46	32
96	17:20:32.24	−35:46:59.42	1.88	6.23	21.3	74.0	0.52	11.0	11.3	56	60
97	17:20:31.99	−35:46:35.44	1.51	3.06	19.1	36.4	0.64	12.0	12.3	60	60
98	17:20:31.98	−35:58:41.43	0.45	0.44	11.1	5.2	0.48	14.9	16.7	60	60
99	17:20:31.98	−36:01:08.43	0.69	2.62	23.1	31.1	0.53	10.9	8.8	52	24
100	17:20:31.51	−35:46:14.43	0.41	1.33	19.5	15.8	0.44	12.6	9.9	60	33
101	17:20:31.25	−35:48:35.43	0.90	1.20	13.4	14.3	0.51	12.0	12.2	60	60
102	17:20:30.51	−36:00:56.43	0.81	2.81	20.5	33.4	0.46	12.5	11.9	60	60
103	17:20:30.50	−36:02:29.41	0.34	0.32	10.0	3.8	0.39	14.4	15.6	60	60
104	17:20:30.26	−36:00:05.44	0.50	1.21	17.6	14.4	0.49	10.2	5.4	38	12
105	17:20:29.52	−35:48:14.42	0.47	1.19	17.0	14.1	0.43	15.0	16.7	60	60
106	17:20:28.27	−36:00:59.41	0.32	0.31	9.7	3.6	0.34	14.4	14.8	60	60
107	17:20:28.02	−35:59:05.43	0.40	0.39	10.3	4.6	0.40	4.2	1.1	9	5
108	17:20:28.02	−35:58:53.42	0.42	0.58	12.2	6.8	0.40	5.9	5.5	13	12
109	17:20:27.55	−35:52:47.41	1.76	8.46	26.7	100.5	0.56	11.7	10.5	60	42
110	17:20:27.53	−36:01:05.41	0.35	0.32	9.6	3.7	0.35	12.5	14.7	60	60
111	17:20:27.32	−35:45:26.42	0.44	1.56	20.6	18.6	0.45	8.2	6.4	20	14
112	17:20:27.30	−35:53:05.42	1.55	3.07	15.2	36.5	0.44	11.7	10.6	60	44
113	17:20:27.29	−35:58:38.41	0.30	0.33	10.6	3.9	0.35	6.3	1.6	14	6
114	17:20:26.54	−36:01:14.40	0.55	1.79	20.0	21.2	0.47	12.4	14.2	60	60
115	17:20:25.82	−35:53:11.42	1.26	2.13	14.2	25.3	0.45	11.3	11.3	60	60
116	17:20:25.81	−35:58:20.41	0.32	0.40	11.2	4.7	0.36	7.6	6.1	18	13
117	17:20:25.34	−35:45:05.41	0.49	0.80	14.2	9.5	0.47	7.6	5.6	18	12
118	17:20:25.06	−36:00:26.39	0.38	0.40	10.7	4.8	0.40	14.1	12.8	60	60
119	17:20:24.83	−35:53:11.40	1.34	3.48	16.8	41.4	0.39	11.0	11.0	53	56
120	17:20:24.34	−35:52:35.41	0.48	1.23	15.7	14.7	0.31	9.1	5.8	26	12
121	17:20:24.08	−35:54:56.39	8.78	51.31	36.1	609.7	0.71	11.8	11.7	60	60
122	17:20:24.07	−35:59:05.41	0.48	1.63	20.2	19.3	0.46	3.4	0.9	8	5
123	17:20:23.62	−35:45:05.40	0.52	0.42	10.4	5.0	0.52	6.9	6.0	15	13

Table 1
(Continued)

Name[a]	R.A.[b]	Decl.[b]	Peak[c]	Total[c]	Radius[c]	Mass[d]	Concentration[c]	450/850 μm Ratio[e]		$T(p)$[e]	$T(s)$[e]
	(J2000)	(J2000)	(Jy beam^{-1})	(Jy)	(arcsec)	($M_\odot$)		Peak	Total	(K)	(K)
(1)	(2)	(3)	(4)	(5)	(6)	(7)	(8)	(9)	(10)	(11)	(12)
124	17:20:23.35	−35:53:44.40	1.15	6.07	26.1	72.1	0.49	10.9	12.7	51	60
125	17:20:22.35	−35:55:38.37	3.09	18.21	33.7	216.3	0.66	10.9	11.2	51	60
126	17:20:22.12	−35:52:53.39	0.67	1.64	17.3	19.5	0.47	11.2	6.1	60	13
127	17:20:22.11	−35:58:17.39	1.28	3.88	21.7	46.2	0.58	10.8	9.7	50	31
128	17:20:20.14	−35:52:59.36	0.29	0.32	10.4	3.9	0.33	11.6	4.0	60	9
129	17:20:19.66	−35:48:41.37	0.44	1.21	17.6	14.4	0.42	14.9	12.6	60	60
130	17:20:19.63	−35:58:44.39	1.47	6.00	25.0	71.4	0.57	8.3	6.6	21	14
131	17:20:19.39	−35:54:38.39	15.23	59.55	29.1	707.7	0.70	9.8	10.7	32	47
132	17:20:19.39	−35:56:35.38	1.62	5.18	24.3	61.5	0.64	13.7	15.7	60	60
133	17:20:18.38	−36:00:41.35	0.42	0.28	8.6	3.3	0.41	18.9	21.4	60	60
134	17:20:18.16	−35:54:44.36	15.03	57.48	27.5	683.1	0.67	9.9	10.5	34	43
135	17:20:17.17	−35:56:50.35	0.82	2.50	19.1	29.7	0.45	14.6	13.7	60	60
136	17:20:17.15	−35:59:05.36	2.37	6.67	20.6	79.2	0.56	7.5	6.6	18	14
137	17:20:15.42	−35:59:29.33	2.75	9.20	23.4	109.3	0.60	7.9	7.1	19	16
138	17:20:15.19	−35:54:50.34	3.15	11.09	22.7	131.8	0.55	11.9	10.9	60	50
139	17:20:14.69	−35:57:20.33	0.39	0.56	12.3	6.7	0.38	11.9	13.1	60	60
140	17:20:14.69	−35:56:35.31	1.37	3.82	20.0	45.4	0.55	11.1	12.4	59	60
141	17:20:13.95	−35:58:41.32	1.28	4.20	23.9	49.9	0.62	5.3	2.8	11	7
142	17:20:13.71	−35:55:56.32	1.56	4.58	20.8	54.4	0.56	13.3	14.4	60	60
143	17:20:13.46	−35:55:29.32	1.34	5.75	23.9	68.3	0.51	13.2	12.2	60	60
144	17:20:13.23	−35:53:02.31	0.26	0.39	11.6	4.7	0.26	6.7	2.0	15	6
145	17:20:13.22	−35:54:47.32	2.30	5.29	17.2	62.8	0.49	11.2	11.0	60	53
146	17:20:12.95	−35:59:02.31	1.08	3.59	21.5	42.6	0.53	5.6	3.4	12	8
147	17:20:11.50	−35:54:47.29	3.28	8.35	20.9	99.2	0.62	11.3	10.8	60	49
148	17:20:09.77	−35:54:50.25	3.45	16.90	34.6	200.8	0.73	11.3	9.9	60	33
149	17:20:09.24	−35:58:32.25	0.71	0.87	12.7	10.3	0.50	4.0	1.4	9	5
150	17:20:07.76	−35:58:29.25	0.90	1.09	12.8	12.9	0.51	4.4	2.4	10	7
151	17:20:04.55	−36:00:02.20	0.54	2.54	23.5	30.1	0.44	10.5	10.1	42	35
152	17:20:02.82	−35:59:05.15	0.42	0.28	9.0	3.3	0.47	0.0	0.0	...	...
153	17:20:00.37	−35:55:41.11	0.45	0.38	10.4	4.6	0.49	9.8	8.0	32	19
154	17:19:57.91	−35:55:50.07	0.51	0.54	11.7	6.5	0.49	9.6	9.1	30	25
155	17:19:57.64	−35:57:50.06	23.22	70.09	35.6	833.0	0.84	10.2	10.0	37	34
156	17:19:56.44	−35:53:20.06	0.36	0.91	16.5	10.8	0.39	0.0	0.0	...	...
157	17:19:55.66	−35:57:47.02	9.79	61.12	35.4	726.3	0.67	12.2	11.1	60	58
158	17:19:54.42	−35:58:35.01	1.07	4.67	26.2	55.5	0.58	9.2	6.9	26	15
159	17:19:53.40	−36:02:19.98	0.46	0.62	12.7	7.4	0.45	9.6	10.2	30	37
160	17:19:52.97	−35:55:52.97	0.32	0.60	13.4	7.1	0.32	10.0	4.3	34	10
161	17:19:52.66	−36:02:19.97	0.51	0.51	11.5	6.1	0.50	9.7	9.1	31	25
162	17:19:51.98	−35:56:04.95	0.32	0.24	9.0	2.8	0.39	11.6	6.0	60	13
163	17:19:51.96	−35:57:07.94	2.01	9.55	27.3	113.5	0.58	9.6	8.4	30	21
164	17:19:51.72	−35:56:22.95	0.35	0.38	10.6	4.5	0.36	7.9	10.0	19	35
165	17:19:50.92	−36:02:22.93	0.36	0.44	11.7	5.2	0.42	12.9	9.5	60	29
166	17:19:47.77	−35:57:31.86	0.87	4.61	25.0	54.7	0.44	10.2	6.2	37	13
167	17:19:44.81	−35:56:04.78	1.14	2.54	17.4	30.2	0.52	11.0	9.8	56	32
168	17:19:40.60	−35:56:55.66	0.77	0.92	12.5	10.9	0.50	4.8	0.8	10	4

Notes.
[a] Clump number.
[b] Position of peak surface brightness within clump (accurate to 3″).
[c] Peak flux, total flux, radius, and concentration are derived from `clfind` (Williams et al. 1994). The peak and total fluxes have uncertainties up to 20% at 850 μm, mostly due to flux calibration. The radius has not been deconvolved with the telescope beam. The concentration was calculated using Equation (3).
[d] Clump masses calculated assuming a constant temperature of 25 K, a dust opacity of 0.02 cm^2 g^{-1} and a distance of 1700 pc (see Equation (2)).
[e] Ratio of fluxes at 450 and 850 μm and the temperature inferred. Temperatures were calculated to a maximum of 60 K; those above 22 K are not well determined in an absolute sense. See Section 6 for further details.

significant portion of the error in R is due to calibration errors, which are expected to be roughly constant across the map. We therefore include temperatures up to 60 K in our tabulation and plots, while noting that the actual values should be regarded with substantial caution.

With the preceding caveats Figure 8 shows the distribution of temperatures for the clump ensemble. While we observe a large dispersion in the derived values for both the peak and integrated flux densities, in principle the latter should provide a more reliable result. Excluding clumps with derived temperatures

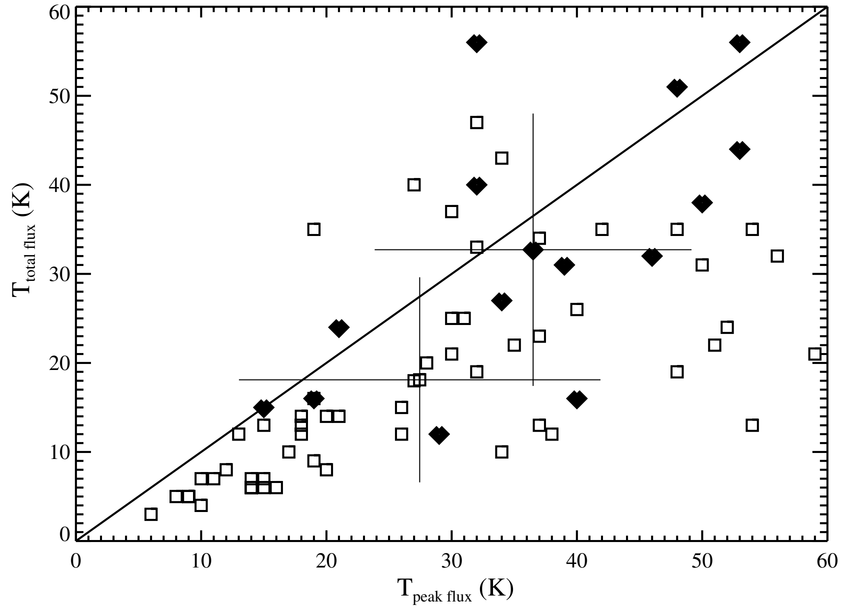

Figure 8. Temperatures for the dust clumps observed in NGC 6334 derived using the integrated 450 μm/850 μm flux density ratio vs. that derived from the peak values. Clumps which lie on the diagonal line have equal peak and integrated values. Clumps which lie within the narrow ridge of submillimeter-wavelength emission are differentiated by the filled symbols, as compared with the "field" clumps, for which the open squares are used. The large crosses indicate the mean values of the peak and total temperatures derived from the two populations of clumps. The extents of the two crosses indicate the rms range of values; there is considerable overlap between the two populations of clumps, and no clear differentiation between them in terms of temperature.

of $T \geqslant 60$ K (see above), we obtain a mean temperature of $\sim$25 K for the entire clump ensemble from the integrated flux density ratios, assuming a spectral index β of 2. In Figure 8 we indicate the mean positions and rms extents of the two clump distributions differentiated on the basis of membership either within the ridge emission or in the larger field of NGC 6334. Statistically, however, the two populations are not significantly distinct in their properties.

Finally, following Johnstone et al. (2001), we derive the masses given in Table 1 from the relation

$$M_{\rm clump} = 11.8 \times S_{850} \left[\exp\left(\frac{17\,{\rm K}}{T_d}\right) - 1 \right] \left(\frac{\kappa_{850}}{0.02\,{\rm cm^2\,g^{-1}}} \right)^{-1} \times \left(\frac{d}{1700\,{\rm pc}} \right)^2 M_\odot \qquad (2)$$

in which we assume that the observed emission arises from optically thin dust particles having a single value for the temperature T_d of 25 K and a dust opacity κ_{850} of 0.02 cm^2 gm^{-1}. We employ a gas-to-dust ratio of 100, and use the adopted distance d for NGC 6334 of 1.7 kpc obtained by Neckel (1978).

The degree of central concentration (C_d; Column 8) was obtained using the relation

$$C_d = 1.0 - \left[\frac{1.13 B^2 S_{850}}{\pi R_{\rm obs}^2 f_0} \right], \qquad (3)$$

where B is the beam size to half-power, S_{850} is the total flux density, $R_{\rm obs}$ is the clump radius, and f_0 is the peak flux density, as in, e.g., Johnstone et al. (2001). The value of C_d has implications for the stability of a given clump if we were to interpret the results in the context of the Bonner–Ebert (BE) sphere formulation (Bonnor 1956; Ebert 1955), as in, e.g., Johnstone et al. (2006). This model allows a relatively simple analytical treatment of a complex issue, by assuming that gas or dust clumps can be considered as spherical isothermal objects bounded by external pressure, and in which thermal pressure is balanced by gravity. Objects with low values of $C_d \leqslant 0.33$ have uniform density and are not prone to gravitational collapse, whereas objects with large values of $C_d \sim 0.72$ are expected to be undergoing collapse under self-gravity.

In the present analysis we find that 12 clumps satisfy the former instance, with a mean value of $C_d \sim 0.3$. Most of these objects have derived masses at the low end of the distribution, typically a few $M_\odot$ at most. Two clear exceptions, clumps 46 and 62 in Table 1, have masses of order 100 $M_\odot$. At the other extreme, the most massive clumps preferentially have the largest values of C_d, implying that these objects may be undergoing collapse under self-gravity. A histogram of the C_d values grouped into 0.05 wide bins shows a well-defined symmetric distribution centered at $C_d \sim 0.43$ with an FWHM of about 0.3. This behavior is similar to that reported for the Perseus region, but differs from that found in the Ophiuchus cloud by Jørgensen et al. (2008).

6.1. Clump Distributions with Temperature

Although there is substantial uncertainty in determining dust temperatures the distribution of apparently warmer clumps (those with high flux density ratios) does not appear to be entirely random. Many of the clumps with high flux ratios are associated with relatively weak emission, i.e., measurement errors have a strong influence on the results. However, a substantial number of the brighter clumps for which high ratios are derived are significantly clustered. In particular, all of the brightest clumps in NGC 6334 I and I(N) have high flux ratios, from our 850/450 μm observations. This also applies to the three successive clumps within the ridge of emission closest to the I/I(N) complex. In source IV, four of the six clumps forming the loop to the south similarly indicate higher temperatures, and the first clump in the ridge to the north of source IV likewise falls in this category. In contrast, the flux ratios of the eight clumps within the main body of source IV itself are all lower, although the flux ratios are still too high for determination of a reliable temperature. Source V, further to the south, contains no clumps possessing large flux ratios, while the ridge of emission between I/I(N) and IV shows no especially warm clumps other than those which are noted in relation to I/I(N) and IV.

A similar separation of the coolest clumps (those for which $T(s) \leqslant 15$ K) shows no major features regarding distribution, with the possible exception of a grouping of medium-sized clumps that occurs about 4′ south of Source IV. Within the narrow emission ridge there is a small group of three apparently colder clumps north of source I(N), and one near source III.

6.2. Clump Masses

The summed mass (assuming a dust temperature of 25 K) found in the NGC 6334 field is about 16700 $M_\odot$; half of this is contained within the seven most massive clumps. As shown in Figure 9, the most massive of the latter objects is associated with NGC 6334 I(N), followed by source I, with masses of about 2800 and 2000 $M_\odot$, respectively. Note that recent observations of source I(N) suggest that it may be much hotter, ∼170 K (Beuther et al. 2008), which would imply a much lower total mass for the same observed total flux. Three major clumps are associated with NGC 6334 IV, totaling 2000 $M_\odot$, and two with NGC 6334 V, for an additional 1560 $M_\odot$. There are no massive dust clumps associated with either sources II or III, although clumps are located close to the *IRAS*-PSC positions of both objects (see Figure 4), with estimated masses of 54 and 33 $M_\odot$ respectively. Source II also coincides with an *IRAS*-PSC object, while source III is displaced from a nearby *IRAS*-PSC object, which in turn is coincident within the *IRAS* pointing errors with a relatively substantial clump (object 95 in Table 1) with a mass of 280 $M_\odot$ located within the ridge of dust emission.

Figure 11 shows the distribution of mass versus number of the dust clumps in NGC 6334. For the higher clump masses these data imply a cumulative mass index $N(M) \propto M^x$ ([9]) where x is between −1.5 and −1.0 for the higher masses, and exhibits a substantial flattening of this relationship for masses below about 50 $M_\odot$.

For comparison, of the other star-forming regions which have been subjected to clump-finding analyses, NGC 6334 is most similar to NGC 7538 (Reid & Wilson 2005), in that the most massive clumps in both regions have masses between 2000 and 3000 $M_\odot$. The lower limits of clump detection in both NGC 6334 and NGC 7538 are also similar, about 1 $M_\odot$, although the clump distribution is expected to be substantially incomplete at these lower masses in the present case. This is in contrast with the nearby star-forming regions such as ρ Ophiuchus and Orion B, where the distances to the clouds are small enough that cores with the potential to form a single star, or small number of stars ($M < 10\ M_\odot$), can be resolved.

Figure 10 shows the masses and radii of all of the clumps identified in NGC 6334. This figure indicates that most of the higher-mass clumps are too massive to be supported by thermal pressure alone (indicated by the dashed line), and require additional support from turbulent motions or magnetic fields if they are to be stable against collapse. This result still holds even if a somewhat larger thermal temperature were assumed—many of the clumps require temperatures of at least 50 K for thermal support alone to prevent gravitational collapse.

[9] This relation is often expressed in its differential form $dN/dM \propto M^{(-x-1)}$ or $dN/d\log M = dN/dM \times M$.

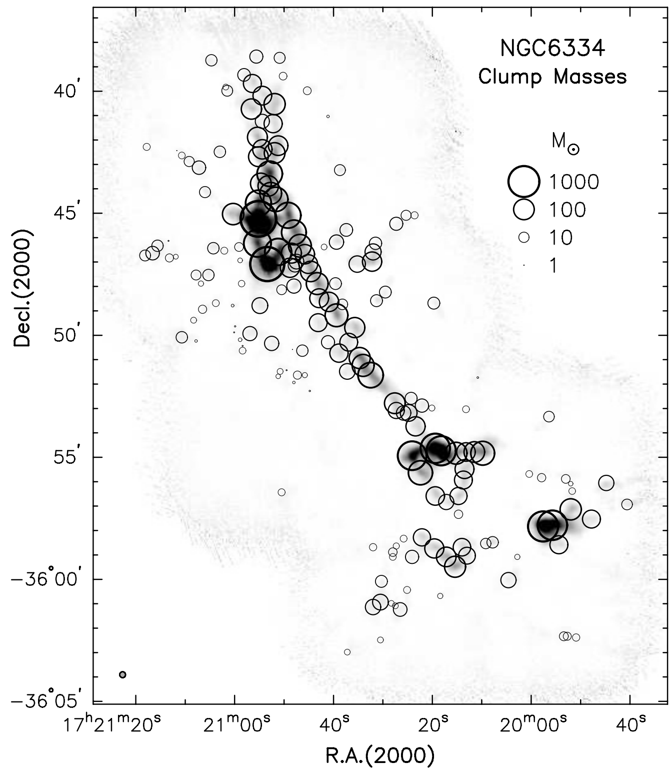

Figure 9. The distribution of mass in NGC 6334 obtained from the present data. Each clump is represented by a circle, the diameter of which is proportional to the logarithm (to base 10) of the mass $M_\odot$ derived assuming a dust temperature of 25 K. Representative mass icons are shown in the key in the upper right; a mass of 1 $M_\odot$, at the lower limit of detected clumps, is barely visible in this image. The underlying image, and other details are as in Figure 7.

6.3. The “Backbone” of NGC 6334

The ridge of emission seen in NGC 6334 at submillimeter wavelengths is a striking feature (see Figures 1–4). Already clearly evident, as noted by Sandell (2000) in his “cobweb” paper, it runs along the west side of the dense I/I(N) complex, and there are hints of this feature in the early 400 μm image of this region obtained by Gezari (1982) using the Infrared Telescope Facility (IRTF) on Mauna Kea. The present large-scale images of NGC 6334 show that this structure extends from source IV to at least 5′ north of source I(N), where it appears to bifurcate. Overall, this structure gives the impression that it may have some physical significance in the context of star formation in NGC 6334.

Inspection of the NGC 6334 ridge in the present images shows some interesting features of the dust distribution. Lateral excursions from the overall line of the ridge appear between sources II and III, and just north of source IV, where the ridge terminates. The ridge is mostly spatially resolved with the present observations, and reaches peak flux densities at 850 μm of 20 Jy beam^{-1}. Further, with a summed mass estimated from the current clump ensemble of about 3770 $M_\odot$ it contains a substantial fraction of the total mass of cold dust observed in NGC 6334.

The `clfind` results tend to support the suggestion that the ridge is different in character from the rest of the NGC 6334 star-formation region. Figures 10 and 11 show the individual clumps differentiated on the basis of location along the ridge or in the field of NGC 6334, respectively. From these data it would appear that the clump mass spectrum of the ridge component

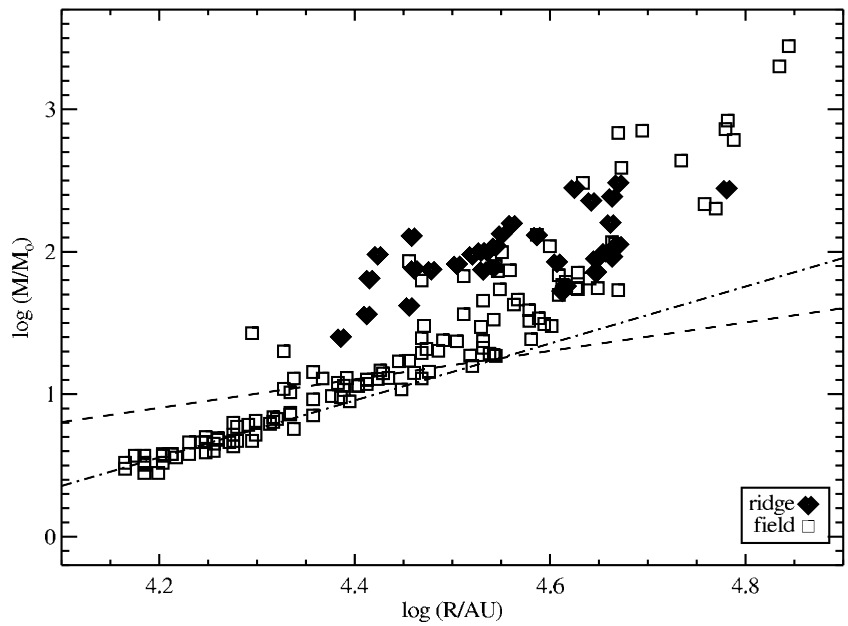

Figure 10. The derived distribution of dust clump masses in NGC 6334 as a function of radius. Clumps found in the emission ridge are differentiated from those in the NGC 6334 field by the filled diamond symbols and the open square symbols, respectively. The dashed line indicates the virial equilibrium relation for a temperature of 25 K, while the dash-dotted line indicates the minimum observable sensitivity to mass.

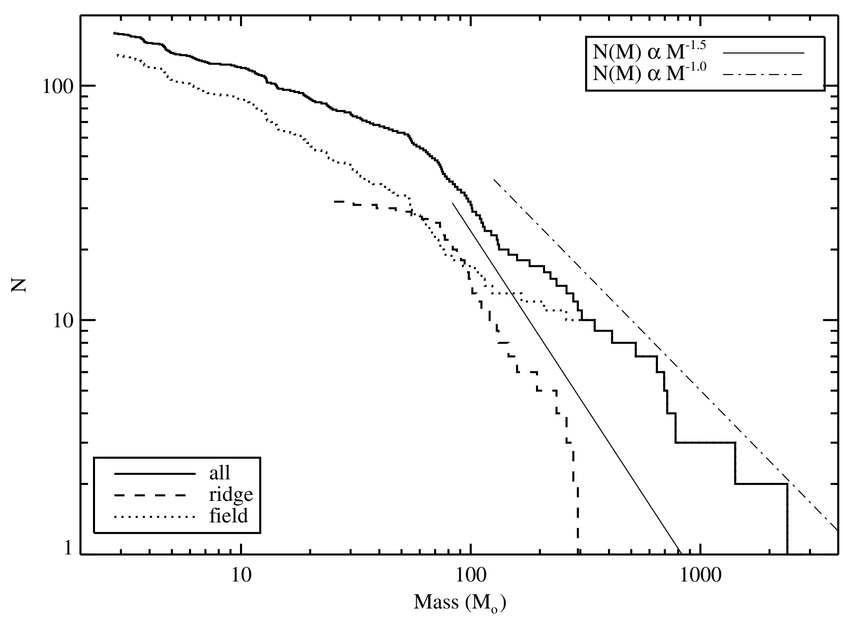

Figure 11. Cumulative mass–number relations for dust clumps found in NGC 6334, differentiated on the basis of membership in the ridge of submillimeter continuum emission ("ridge"), field clumps ("field"), and the total clump distribution ("all"), as shown by the key in the box in the lower left. Two representative number vs. mass slopes are indicated by the solid and dot-dashed lines (see key in the upper right); overall, the mass–number distribution is steeper for clumps in the ridge material than for the "field" clumps.

is distinct from that of the body of NGC 6334. In particular, (1) there are no clumps identified with masses less than about 12 $M_\odot$ in the ridge, (2) the mass–number relationship is notably steeper than that of the field sources, with $N(M) \propto M^{-1.5}$, as opposed to $N(M) \propto M^{-1.0}$ (or even less steep) for the field sources, and (3) the high-mass limit for clumps in the ridge is about 300 $M_\odot$. There is no particular concentration of the ridge clumps when the dust temperatures are considered, within the large uncertainties in the estimated temperatures (see Figure 8).

The significantly narrower ranges of both mass and size for clumps in the ridge with respect to that of the rest of NGC 6334 may be seen as either a result of the physical environment and/or a nonphysical effect stemming from the clump-finding process in the particular geometry of the ridge. Regarding the former, as Sandell (2000) noted from his observations of the region near I/I(N), the ridge appears to break into condensations with a separation of 2–4 times the width of the filament. With respect to the latter, we note that `clfind` will identify clumps as separate objects if the contrast between the clump peaks and intervening valleys is significant in terms of the signal-to-noise ratio σ. If the highest and lowest points in the ridge structure were minimally differentiated (if the peak and valley intensities were, for example, 11.5σ and 11.3σ), then the entire ridge structure would be considered to be a single clump. `clfind`

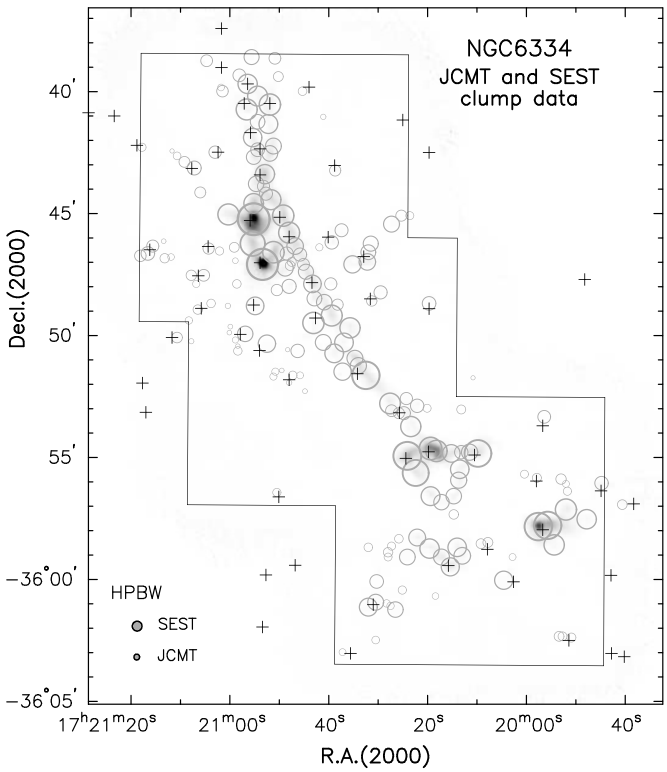

Figure 12. A comparison of the clump distribution found by Muñoz et al (2007) using SEST at 1.2 mm wavelength with that obtained in the present work. The circles represent the distribution of clumps found in the present work, where the sizes of the circles approximate the clump sizes. The crosses indicate the locations of the clumps found by Muñoz et al. (2007); outside the formal 850 μm boundary, where there remains some sensitivity, there are three clump correspondences. The beam sizes (HPBW) of the SEST and JCMT telescopes are given on the lower left.

is, however, very sensitive to intensity variations, and hence if the clump/inter-clump intensity differential is significant, then the structure will be divided into a series of individual clumps. Within the limitations imposed by the observing beam size, we conclude that the ridge structure is a coherent physical entity containing substructures at least to the resolution limit of the present observations. The velocity structure of the ridge, discussed in Section 8.1, supports this view.

7. CLUMP MASS DISTRIBUTIONS—COMPARISONS WITH OTHER DATA

Independent observations of the NGC 6334 region have been reported recently by Muñoz et al. (2007) and can be readily compared with the present work. Their observations were obtained using the SEST at a wavelength of 1200 μm with a beamwidth of 22″. In an area substantially larger than that observed by ourselves they identified a total of 182 clumps. Fifty-two of these lie within the formal border of the 850/450 μm image, with an additional three possible coincidences with clumps just outside the border of the latter, where there is still sufficient sensitivity at 850 μm. Figure 12 compares the distribution of clumps found by Muñoz et al. (2007), overlaid on the distribution we found.

In general, the overall agreement between the clump distributions in the two images is very good, although the larger beamwidth and weaker signal strength at the longer wavelength result in the ridge of emission linking the major dust clumps being less well defined than in the present 850 and 450 μm images. In addition there are frequently instances where structures identified as a single clump by Muñoz et al. (2007) are subdivided in the 850 and 450 μm data. The present 850 μm data identify more than three times as many clumps as within this smaller region, largely a result of the intrinsically stronger emission of individual clumps at 850 μm over that at 1200 μm, and the smaller beamwidth of the present data set.

The total mass determined by Muñoz et al. (2007) from their 1200 μm observations within the region common to both sets of observations is 23,100 $M_\odot$ after correction for free–free emission, more than that obtained in the present work at 850 μm (16700 $M_\odot$). However, the mass is quite sensitive to the dust temperature. In our calculations (Section 6) we adopt a dust temperature of 25 K, although the distribution of the ratio of 450/850 μm total and peak fluxes (Figure 8) permits a substantial range of values. Muñoz et al. (their footnote 2) chose a value of 17 K. If we also were to adopt a temperature of 17 K, the total mass in our 850 μm observations would be increased to about 29,000 $M_\odot$. Given the differing assumptions about dust opacity and the observational uncertainties, we consider that the two mass estimates are compatible.

For comparison with the present discussion, there are a number of studies of the mass function in star-forming regions with which the results for NGC 6334 may be compared. Most low-mass star-forming regions have $N(M) \propto M^{-1}$ to $M^{-1.5}$ (see review by Ward-Thompson et al. 2007). There are fewer studies of mass functions of higher-mass star-forming regions, but some of these indicate a similar relationship still holds (e.g., Reid & Wilson 2005, 2006). We note, however, that Muñoz et al. (2007) find $N(M) \propto M^{-0.6}$ for NGC 6334, measuring the slope from the differential mass function. The latter argue that determining the slope of the mass distribution from the cumulative number rather than the differential number can cause a bias toward a steeper slope due to the small number of objects at the highest masses. For the present data set, we would not expect this to have a large effect on the total mass function, which shows a similar slope for over an order of magnitude, but this could be more significant for our analysis where the clumps are divided into those along the ridge and in the field.

8. KINEMATICS AND GAS TEMPERATURES IN NGC 6334

8.1. Kinematics

As part of a separate project spectral line mapping observations of NGC 6334 in the principal CO (2–1) isotopomers were obtained at the JCMT with a beamwidth of 23″. The $C^{18}O$ (2–1) image of the region, integrated over the velocity range appropriate for NGC 6334, shown in Figure 13, bears a close resemblance to that obtained at 850 μm. The more common CO isotopes are often optically thick and obscure the details of the region, while the $C^{17}O$ lines are rather weak; these data are not included in this paper. In Figure 14 we show a series of velocity slices from the $C^{18}O$ data cube which include most of the region seen in the 850 and 450 μm images, the principal exceptions being the extreme northern and southern sections of the latter images.

These images show that while velocity variations within the continuum emission ridge are small, there are changes over the length of the latter. The ridge exhibits a gap at the more negative velocities near FIR source III, suggesting that the ridge may have been disrupted by the development of this particular object. Otherwise, the ridge as traced by molecular material largely

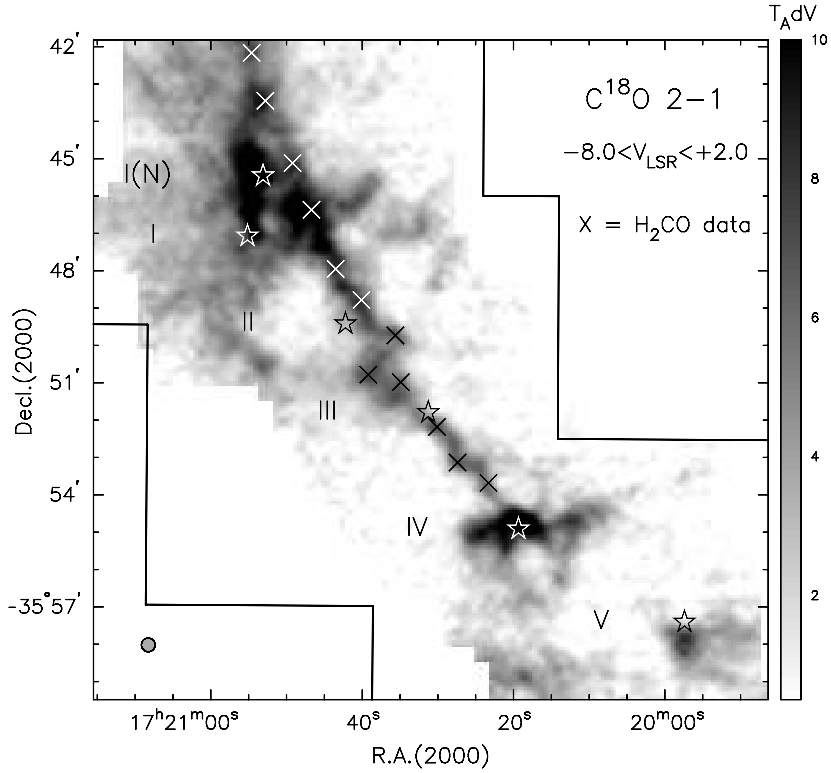

Figure 13. Emission from the $C^{18}O$ (2–1) transition toward NGC 6334 obtained with the JCMT, integrated over the velocity range -8 km s^{-1} $< V <$ +2 km s^{-1} (wrt LSR). The half-power beamwidth (23″) for the $C^{18}O$ observations is shown on the lower left. The positions of the compact FIR sources in the region (Loughran et al. 1986) are indicated by the star symbols, as in Figure 4, for orientation purposes. The extent of the 850 μm image is somewhat greater than that of the $C^{18}O$ (2–1) data, as shown by the boundary in this figure. The 12 positions indicated by "X" were observed in two transitions of H_2CO (see Section 8.2 and Table 2) with the same beamwidth to obtain estimates of the gas temperature. CH_3OH (4_{23}–3_{13}), included within the spectral band covered by these spectra, was detected in the six northern positions only.

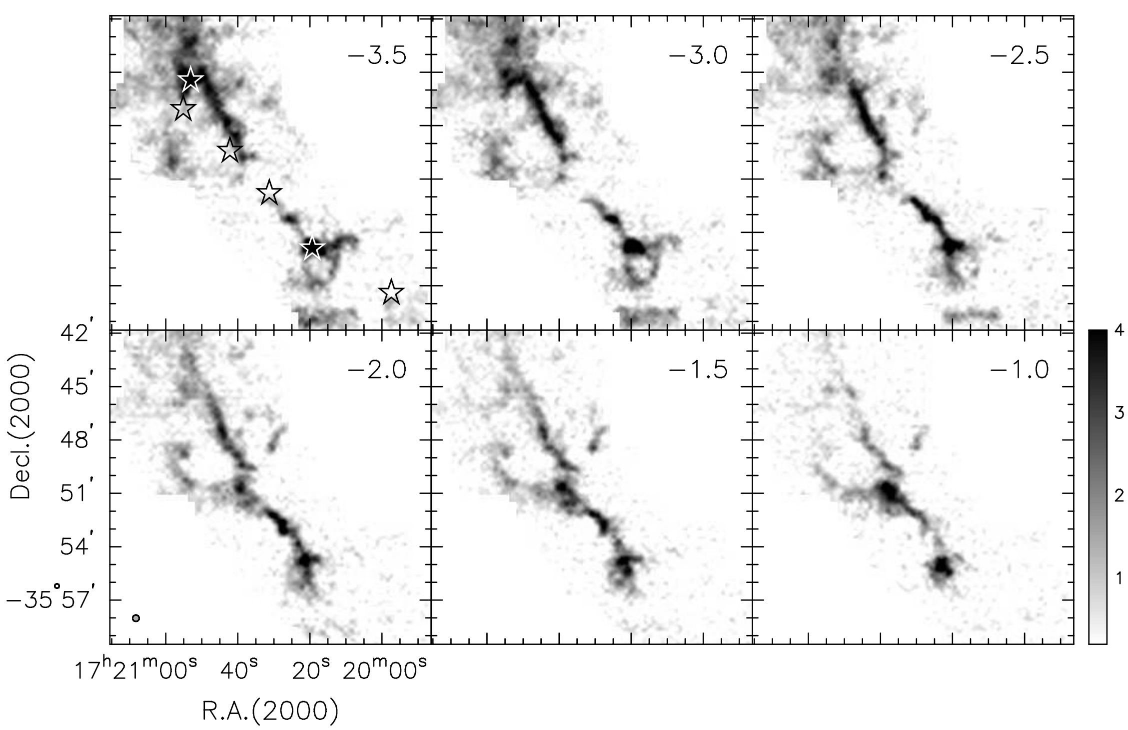

Figure 14. A series of velocity slices (0.5 km s^{-1} width) from the data cube of the $C^{18}O$ (2–1) transition toward NGC 6334 (see also Figure 13 and the text), showing significant changes in the gas distribution over rather small velocity intervals. The central velocity with respect to the LSR is given in the upper-right corner of each panel. The positions of the compact FIR sources in the region (Loughran et al. 1986) are indicated in the upper-left panel. The half-power beamwidth for these observations is again shown in the lower left of the bottom-left panel.

maintains a fairly constant LSR velocity throughout its length. Integrating the $C^{18}O$ (2–1) emission over the LSR velocity range from −8 to +2 km s^{-1}, as in Figure 13, shows that, while there are some differences in detail between the submillimeter-wavelength continuum and millimeter-wavelength spectral line images, the close overall correspondence indicates that the dust and gas components are co-spatial.

8.2. Gas Temperatures

We obtained spectra simultaneously of two transitions of H_2CO at 12 positions along the ridge of NGC 6334 in order to estimate the gas temperature. These spectra also include the 4_{23}–3_{13} transition of CH_3OH, and all three spectral lines share a similar noise level within each spectrum. The positions observed (see Figure 15) cover the entire ridge from just north of FIR source IV through the apparent extension of the ridge north of sources I and I(N). The spacing between neighboring observations is typically 1′ or 2′. They sample potentially different external local heating conditions due to the proximity or otherwise of H II and star-forming regions at each location.

The results of these observations are summarized in Table 2, where the entries are listed in order of decreasing (i.e., more negative) declination. For each position we list the integrated line intensities for both H_2CO transitions and that of CH_3OH. For the H_2CO (3_{03}–2_{02}) transition, which has the best S/N for the three observed transitions, we characterize the spectra with Gaussian fits in terms of peak intensity, width at half-power, and central velocity. In five cases the single-Gaussian fit is quite poor, and a two-component (given by A and B) fit is suggested in these cases. The higher-excitation H_2CO ($3_{22} - 2_{21}$) line is detected at all positions although the S/N is marginal in some cases. The CH_3OH (4_{23}–3_{13}) transition is detected only in the six northernmost positions (entries 1–6 in Table 2), and is especially strong at position 2, in the apparent extension of the ridge 2′ north of the FIR source I(N). The lack of detections of CH_3OH in the southern part of NGC 6334, compared with H_2CO, which is found through NGC 6334, is notable, and may be a density-related effect.

The LTE temperatures of the gas component of the emission ridge estimated on the basis of the H_2CO data range from about 35–70 K, in two main groupings centered at about 40 and 55 K (see Table 2). The most extreme values are for the southern-most position 1 just north of source IV (70 K), and position 9, in close proximity to I(N) (35 K). These temperatures are not inconsistent with the rather large range derived for the dust clumps. As for the submillimeter continuum data the H_2CO temperatures are poorly determined at the more extreme temperatures.

8.3. Gas Column Density

The $C^{18}O$ (2–1) data allow us to estimate the total gas column densities within NGC 6334 using the relation given by Equation (10) in Shirley et al (2005) (see Goldsmith & Langer 1999 for a detailed discussion). For the present purpose this relation becomes

$$N(C^{18}O) = 5.8\times10^{14}\frac{\tau}{1-\exp^{-\tau}}\int\frac{T_A^* dv}{\eta_{\rm mb}}, \qquad (4)$$

where τ is the optical depth in the spectral line, $T_A^* dv$ is the integrated spectral line intensity (units of K km s^{-1}), and $\eta_{\rm mb}$ is the main-beam efficiency (about 0.65).

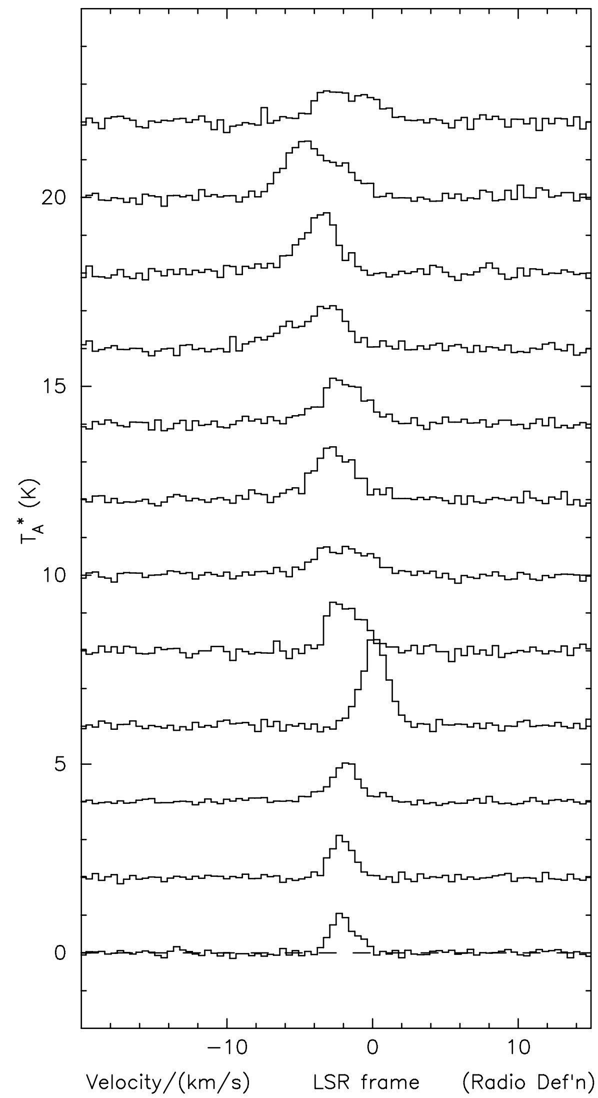

Figure 15. Spectra of the H_2CO ($3_{03} - 2_{02}$) transition observed at 12 locations within the elongated ridge of continuum and molecular emission from NGC 6334 (see Figure 13). The spectra are arranged in order of the declination of each observed point (south is at the bottom), and aligned on a common velocity scale. See Table 2 for integrated intensities and Gaussian-fit parameters for these data.

The $C^{18}O$ optical depth varies substantially across NGC 6334, but does not saturate. With integrated intensities of typically ∼5–10 K km s^{-1} in T_A^* we estimate the $C^{18}O$ column density to be 5–10 $\times10^{15}$ cm^{-2}. The total (H_2) column density can also be estimated from the 850 μm map; a flux of 1 Jy $beam^{-1}$ (typical of the emission on the ridge) corresponds to a total column density of 4.5 × 10^{22} cm^{-2}. This in turn implies a $C^{18}O$ abundance of $\sim10^{-7}$. The latter value is typical of those found in the ISM; for instance, Tafalla et al. (2004) find that the outer parts of L1498 and L1517B can be well characterized by $C^{18}O$ abundances of 0.5 and 1.7×10^{-7}, respectively. This suggests also that, on the physical scale of the ridge in NGC 6334, there is very little freeze-out or depletion of CO.

9. CONTRASTING SUBMILLIMETER- AND MIR WAVELENGTH IMAGES

The *MSX* (see Price et al. 2001) mapped the Galactic plane in four MIR bands with an angular resolution of 18″ and

Table 2
Observations of H_2CO and CH_3OH Transitions Toward NGC 6334

Observation		R.A. (J2000)	Decl. (J2000)	H_2CO (3_{03}–2_{02}) (K km s^{-1})	Gaussian Fits Peak (K)	Width (km s^{-1})	V(LSR) (km s^{-1})	H_2CO (3_{22}–2_{21}) (K km s^{-1})	T_{kin} (K)	CH_3OH (4_{23}–3_{13}) (K km s^{-1})
1		17:20:54.6	−35:42:10	4.07 ± 0.15[a]	0.81	4.9	−1.9	0.72 ± 0.14[a]	41	1.02[a]
	A[b]				0.75	2.8	−3.0			
	B[b]				0.62	2.6	−0.5			
2		17:20:52.8	−35:43:27	6.71 ± 0.14	1.39	4.6	−4.2	1.63 ± 0.16	57	3.99
	A				1.20	2.6	−5.1			
	B				0.89	3.5	−2.6			
3		17:20:49.2	−35:45:07	5.68 ± 0.15	1.51	3.1	−3.7	0.98 ± 0.15	40	0.93
	A				0.12	5.6	−6.9			
	B				1.45	3.1	−3.6			
4		17:20:46.7	−35:46:22	5.34 ± 0.13	1.02	4.7	−3.7	0.75 ± 0.15	34	1.44
	A				0.47	3.3	−6.2			
	B				1.11	2.9	−3.0			
5		17:20:43.5	−35:47:57	4.91 ± 0.13	1.16	3.5	−2.0	0.89 ± 0.13	42	0.80
6		17:20:40.1	−35:48:47	5.28 ± 0.12	1.33	3.3	−2.6	1.15 ± 0.13	51	0.75
7		17:20:35.6	−35:49:44	3.81 ± 0.12	0.72	4.7	−2.0	0.88 ± 0.13	54	...[c]
8		17:20:39.2	−35:50:47	3.73 ± 0.15	1.27	2.8	−1.9	0.60 ± 0.14	38	...
	A				1.21	2.4	−2.1			
	B				0.30	2.2	−0.6			
9		17:20:34.9	−35:50:59	5.41 ± 0.12	2.35	2.1	+0.2	1.29 ± 0.14	56	...
10		17:20:30.1	−35:52:11	2.89 ± 0.09	0.97	2.5	−1.9	0.47 ± 0.08	38	...
11		17:20:27.4	−35:53:08	2.03 ± 0.08	1.06	1.8	−2.1	0.46 ± 0.09	52	...
12		17:20:23.3	−35:53:41	1.92 ± 0.08	0.97	2.0	−2.1	0.55 ± 0.08	72	...

Notes.
[a] Integrated line intensities for the molecular transition indicated.
[b] H_2CO spectra were fitted with two Gaussians where "A" and "B" are indicated.
[c] CH_3OH emission not detected above the noise level at positions (7–12) for which no integrated intensity is given.

thus provides a compatible comparison with the submillimeter-wavelength images presented here. The 8.3 μm (band A) images are often dominated by fluorescence from PAHs, particularly when the 12.1 μm image (band C) shows the same morphology. Band E, centered about 21.3 μm, shows primarily the emission from silicate and other dust at temperatures of typically 100 K or more. Recently, images have been released from the *Spitzer* GLIMPSE-II mission, which covers four bands centered near 3.3, 4.5, 5.8, and 8.2 μm. The latter data are of much better quality and resolution than the equivalent *MSX* data, although the 12.1 and 21 μm *MSX* images remain the only data at these longer wavelengths. Here we compare these data sets with the SCUBA images.

In Figure 16 we compare images of the NGC 6334 region at NIR and MIR wavelengths with that at 850 μm. Clearly, the overall structure seen in cold dust at submillimeter wavelengths bears very little resemblance to that seen in warm dust at the shorter wavelengths. This is not surprising given that the wavelengths differ by a factor of 100 or more. However, there are some interesting features which show the interplay between the warm dust seen by the *MSX*/*Spitzer* and the cold dust seen by the SCUBA.

We expect that the 8.2 μm emission traces PAH distribution in photodissociation regions with moderate extinction ($As_v \sim$ 1–2 mag), on the surfaces of dark clouds. In contrast, the 21 μm emission indicates regions of active star formation in which the surrounding dust is warmed by embedded young stars. For instance, the extended region of 21 μm emission to the west of the I/I(N) complex is likely to have sufficient dust density that Lyα radiation from stars is resonantly trapped and so maintains thermostatic control over the dust temperature at around 110 K. This contrasts with the more common case of heating by dilute starlight, where the temperature falls as the inverse square root of distance from the star(s). The complementary cases of 8.2 μm PAH and 21 μm warm dust emission leads to the observed wider distribution of the former over the latter, as shown in these two images.

Closer inspection of the NIR images shows some interesting details of the interaction of dust and gas. For example, in Figure 17 a very distinctive section of the narrow ridge of submillimeter-wavelength emission appears in silhouette against the bright NIR background in the GLIMPSE-II images; to some extent this is visible in the *MSX* data also. This part of the ridge is delineated by brighter NIR emission on both sides of the structure, suggesting that dust warmed by external stellar radiation is being evaporated from the surface of the filament. Source III, near the top of this frame, is bright at NIR and MIR wavelengths, but is not represented in cold dust emission. Source IV, however, in the bottom right, shows strong emission at 850 μm corresponding to an apparently bipolar structure at NIR wavelengths, and which appears as three clumps at 21 μm.

A number of other features should be noted. In particular, the ridge of submillimeter-wavelength emission exhibits an apparent break or disruption near a FIR source II (see Figure 16). The latter shows bright emission at the NIR wavelengths, but does not appear to contain a substantial amount of cold dust, as judged from the 850 μm image. Further, in the northern part of NGC 6334 there is substantial emission from the cold dust at 850 μm but rather little at NIR and MIR wavelengths. Source I corresponds to weak NIR/MIR structures, but I(N) is invisible at these wavelengths. A dark band of obscuration is

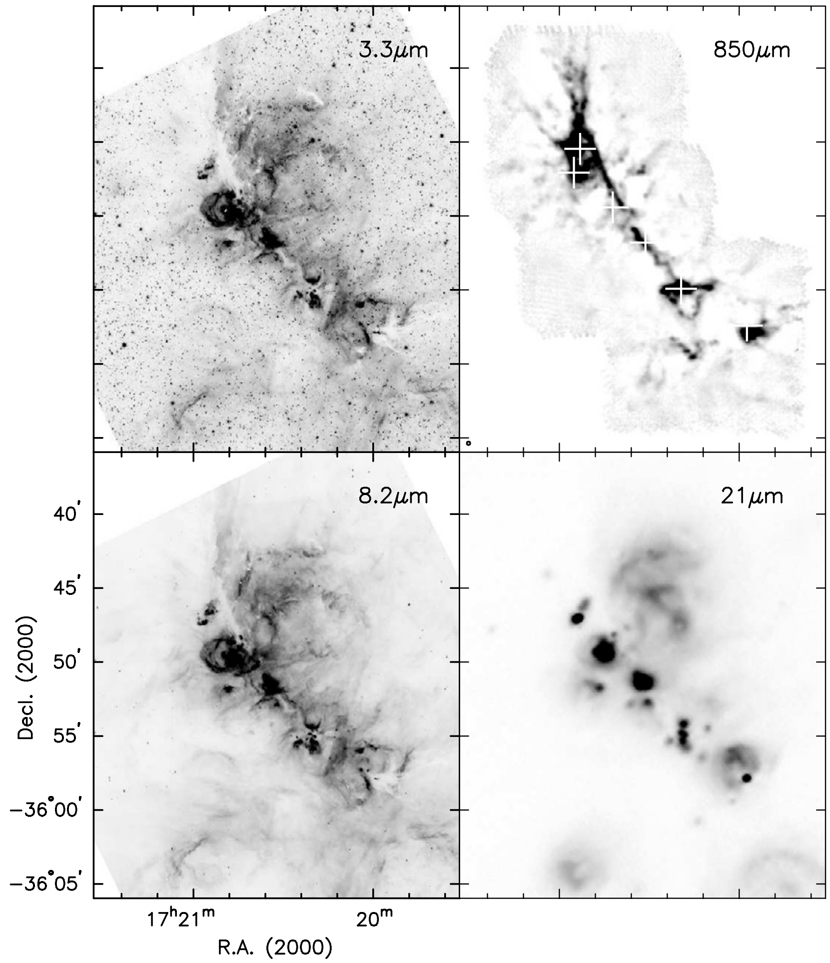

Figure 16. Images of NGC 6334 at IR (3.3 and 8.2 μm; upper- and lower-left panels, respectively; from *Spitzer* GLIMPSE II data) and MIR (21 μm, lower right; *MSX*) wavelengths, compared with the submillimeter (850 μm) image in the top right. For reference purposes the crosses shown in the 850 μm image indicate the positions of the FIR sources found in early observations of the region (see the text). These images cover a similar area to that shown in Figure 5, from the SDSS.

very pronounced in the NIR images in this part of NGC 6334, corresponding to the upper extension of the submillimeter-wavelength emission ridge.

10. CONCLUSIONS

Maps of submillimeter-wavelength emission from the star-forming region NGC 6334 have been compared with MIR and spectral line images made with similar angular resolutions. While the cold dust mapped at 850 and 450 μm is distributed very similarly to the molecular gas revealed by the $C^{18}O$ (2–1) emission, for the most part the relation between the MIR PAH and warm dust shows very few strong correspondences. The differences arise as a result of the origins of the emission; the cold dust forms very compact features perhaps containing pre- or proto-stellar objects, while the MIR emission is the result of illumination or warming from existing young stars.

The observations reveal an ensemble of dust clumps (mostly having masses much greater than 10 $M_\odot$, assuming a temperature of 25 K) which have a mass distribution that lies between roughly $N(M) \propto M^{-1.5}$ and M^{-1}, similar to other star-forming regions. If the clumps are isothermal with a temperature of 25 K, most are too massive to be in virial equilibrium and would require significant support from either turbulent motions or magnetic fields in order to prevent gravitational collapse.

The present observations highlight a prominent ridge of cold dust that can be traced throughout most of NGC 6334, and which appears to have a relatively narrow range of clump parameters when compared with the entire region of NGC 6334. We speculate that this ridge may be a pre-existing feature of the region, and likely in some way to be symptomatic of the processes that drive star formation in NGC 6334, rather than a result of the latter.

The JCMT is operated by the JACH on behalf of the Science and Technology Facilities Council of the United Kingdom, the Netherlands Organization for Scientific Research, and the National Research Council of Canada. The majority of the observations described in this paper were obtained under the Canadian partner queue program M98AC35. We are much indebted to Tim Jenness (JACH) for extensive advice on arcane data reduction issues, and to Doug Johnstone (HIA/NRC Canada) and Remo Tilanus (JACH) for the implementation of matrix inversion used to carry out the latter stages of data reduction at the JACH. Doug Johnstone also provided valuable insight and advice regarding interpretation of the data. We thank Per Friberg (JACH) for information received concerning the properties of the JCMT beam profile. Improvements to an early version of this paper resulted from comments received from William Wall of the Instituto Nacional de Astrofísica Óptica y Electrónica (Mexico). We are also thankful for the insightful comments of the anonymous referee, which have resulted in a more focused discussion of the results obtained in this work.

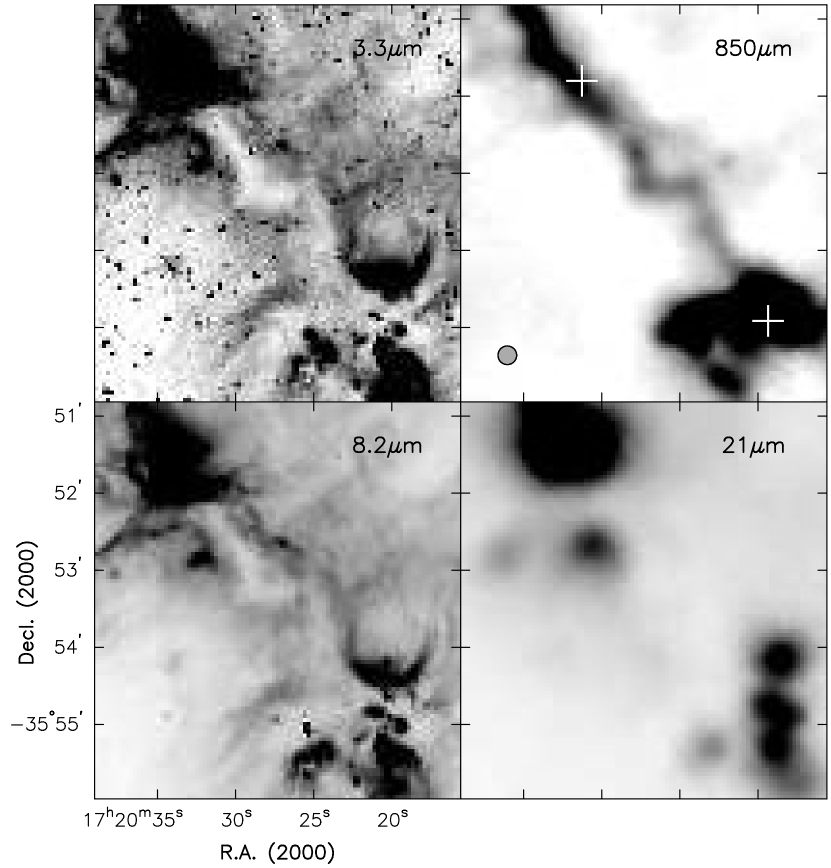

Figure 17. Details from a small section of the *Spitzer* GLIMPSE-II NIR images (at 3.3 and 8.2 μm, respectively; *IRAS*, in the upper- and lower-left panels), compared with the 850 μm (upper right) and *MSX* 21 μm (lower right) emissions. FIR sources III and IV are indicated by the crosses superposed on the 850 μm image in the top left and lower right. A distinctive section of the cold dust seen in emission at 850 μm appears in silhouette against the NIR images. The 21 μm emission has marked differences from the shorter-wavelength images obtained by the *Spitzer*.

H.K. is supported by an NSERC CGSD and an NRC GSSSP award. M.C. thanks NASA for supporting his participation in this work through LTSA grant NAG5-7936 with the University of California at Berkeley.

REFERENCES

André, P., et al. 2000, in Protostars and Planets IV, ed. V. Mannings, A. P. Boss, & S. S. Russell (Tucson: Univ. Arizona Press), 59
Beuther, H., Walsh, A. J., Thorwirth, S., Zhang, Q., Hunter, T. R., Megeath, S. T., & Menten, K. M. 2008, A&A, 481, 169
Bonnor, W. B. 1956, MNRAS, 112, 195
Burton, M. G., et al. 2000, ApJ, 542, 359
Désert, F.-X., Boulanger, F., & Puget, J. L. 1990, A&A, 237, 215
Ebert, R. 1955, Z. Astrophys., 37, 217
Emerson, D. T., Klein, U., & Haslam, C. G. T. 1979, A&A, 76, 92
Gezari, D. 1982, ApJ, 259, L29
Goldsmith, P. F., & Langer, W. D. 1999, ApJ, 517, 209
Holland, W. S., et al. 1999, MNRAS, 303, 659
Jenness, T., & Economou, F. 1999, in ASP Conf. Ser. 172, Astronomical Data Analysis Software and Systems VIII, ed. D. M. Mehringer, R. L. Plante, & D. A. Roberts (San Francisco, CA: ASP), 171
Jenness, T., et al. 2000, in ASP Conf. Ser. 216, Astronomical Data Analysis Software and Systems IX, ed. N. Manset, C. Veillet, & D. Crabtree (San Francisco, CA: ASP), 559
Johnstone, D., Fich, M., Mitchell, G. F., & Moriarty-Schieven, G. 2001, ApJ, 559, 307
Johnstone, D., Matthews, H. E., & Mitchell, G. F. 2006, ApJ, 639, 259
Johnstone, D., Wilson, C. D., Joncas, G., Smith, Gregersen, E., & Fich, M. 2000, ApJ, 545, 327
Johnstone, D., Wilson, C. D., Moriarty-Schieven, G., Giannakopoulou-Creighton, J., & Gregersen, E. 2000, ApJS, 131, 505
Jørgensen, J. K., Johnstone, D., Kirk, H., Myers, P. C., Allen, L. E., & Shirley, Y. L. 2008, ApJ, 683, 822
Kraemer, K. E., et al. 1999, ApJ, 516, 817
Kraemer, K. E., et al. 2000, ApJ, 542, 946
Loughran, L., et al. 1986, ApJ, 303, 629
Mangum, J., & Wootten, H. A. 1993, ApJS, 89, 123
McCutcheon, W. H., et al. 2000, MNRAS, 316, 152
Muñoz, D. J., Mardones, D., Garay, G., Rebolledo, D., Brooks, K., & Bontemps, S. 2007, ApJ, 668, 906
Neckel, T. 1978, A&A, 69, 51
Price, S. D., Egan, M. P., Carey, S. J., Mizuno, D., & Kuchar, T. 2001, AJ, 121, 2819
Privett, G., Jenness, T., Matthews, H., & Barnard, V. 2005, Starlink User Note 213, http://docs.jach.hawaii.edu/star/sun213.htx/sun213.html
Reid, M. A., & Wilson, C. D. 2005, ApJ, 625, 891
Reid, M. A., & Wilson, C. D. 2006, ApJ, 650, 970
Rodríguez, L., et al. 1982, ApJ, 255, 103
Sandell, G. 1999, A&A, 343, 281
Sandell, G. 2000, A&A, 358, 242
Shirley, Y. L., et al. 2005, ApJ, 632, 982
Tafalla, M., Myers, P. C., Caselli, P., & Walmsley, C. M. 2004, A.&A., 416, 191
Ward-Thompson, D., André, P., Crutcher, R., Johnstone, D., Onishi, T., & Wilson, C. 2007, in Protostars and Planets V, ed. B. Reipurth, D. Jewitt, & K. Keil (Tucson: Univ. Arizona Press), 33
Williams, J. P., de Geus, E. J., & Blitz, L. 1994, ApJ, 476, 166
Wright, E. L. 1976, ApJ, 210, 250